

Predicting liquid properties and behaviour via droplet pinch-off and machine learning

Jingtao Wang,^{1,*} Qiwei Chen,^{2,*} C. Ricardo Constante-Amores,² Denise Gorse,³ Alfonso Arturo Castrejón-Pita,^{4,†} and José Rafael Castrejón-Pita^{1,‡}

¹*Department of Mechanical Engineering, University College London, Torrington Place, London, WC1E 7JE, United Kingdom*

²*Mechanical Science & Engineering, University of Illinois Urbana-Champaign, Urbana, IL 61801, United States of America*

³*Department of Computer Science, University College London, London, WC1E 6EA, United Kingdom*

⁴*Department of Engineering Science, University of Oxford, Parks Road, Oxford OX1 3PJ, United Kingdom*

(Dated: February 17, 2026)

Here we demonstrate that the time-evolving interface observed during droplet formation, and consequently the resulting morphology nearing pinch-off, encode sufficient physical information for machine-learning (ML) frameworks to accurately infer key fluid properties, including viscosity and surface tension. Snapshots of dripping drops at the moment of break-up, together with their liquid properties and the flow rate, are used to form a data set for training ML algorithms. Experiments consisted of visualizing, using high-speed imaging, the process of droplet formation by dripping, and identifying the frame closest to break-up. Experiments were conducted using Newtonian fluids under controlled flow conditions. In terms of the Reynolds (Re) and Ohnesorge (Oh) numbers, our conditions cover the domains $0.001 < \text{Re} < 200$ and $0.01 < \text{Oh} < 20$, by using silicon oils, aqueous solutions of ethanol and glycerin, and methanol. For each case, flow parameters were recorded, along with images capturing the final stages of droplet break-up. Supervised regression models were trained to predict fluid parameters from the extracted contours of the breaking droplets. Our data set contains 840 examples. Our results demonstrate that machine-learning models can accurately infer, across a wide range of fluids, key material properties using a single high-speed snapshot taken just before pinch-off. Our methods can predict surface tension, viscosity, or the droplet shape at pinch-off. These approaches provide alternatives to conventional methods to measure liquid properties while reducing measurement complexity and evaluation time and facilitating integration into automation. In addition, unsupervised clustering is performed; the clusters represent regions in the Re–Oh and Bo–Oh planes, indicating that the latent representation may reveal physical properties and offering insight into droplet dynamics.

I. INTRODUCTION

The quantification of liquid properties, such as surface tension, viscosity, and density, is an essential quality-control measure in fluid dispensing processes such as inkjet printing[1, 2] and spray coating [3, 4]. However, some conventional methods for determining fluid properties rely on specialized and complex instrumentation, which often limits their use within small enterprises and complicates automation. Among various existing techniques, the *pendant drop* method has become a widely adopted approach to determine the surface tension of a liquid [5]. In this method, a droplet is suspended from the tip of a capillary, or needle, with the droplet contour recorded by optical imaging. The shape of the pendant droplet, and thus its contour, is controlled by a balance between gravity and interfacial forces [6]. Once the droplet boundary is recorded, numerical solutions of the Young–Laplace equation, which accounts for the pressure difference across the liquid interface, the surface curvature, and surface tension [7], are fitted to determine the surface tension σ [8]. This method is valued for its sim-

licity, small liquid volume requirements, and compatibility with conventional optical imaging systems, making it suitable for both research and industrial environments [9]. In terms of limitations, the pendant drop method relies on the accurate detection of the droplet boundary, which restricts its applicability in cases of low optical resolution, or high image noise, and/or for small droplets [10–12]. Consequently, most setups work with millimetre-sized droplets [10, 12]. Other experimental techniques used to characterise surface tension include the Wilhelmy plate, the Du Noüy ring, and the widely used bubble pressure tensiometry. In the Wilhelmy plate method the surface tension of a liquid is determined by measuring the force exerted by the liquid on a thin fully-wetted plate in contact with its surface [13]. Alternatively, and in a similar fashion, the Du Noüy ring method works by lifting a thin metallic ring from a liquid surface while recording the force required to detach it [13]. These two methods are simple, but their accuracy depends on the skills of the operator and on the use of materials that ensure the complete wetting of the plate or ring. On the other hand, bubble pressure tensiometers are reliable systems that obtain surface tension by measuring the pressure required to produce a bubble at the tip of a capillary submerged in the tested liquid [14]. In this method, the bubble production rate is adjustable, making the technique particularly effective for studying time-dependent interfacial phenomena, such as surfactant diffusion and

* These authors contributed equally to this work.

† alfonso.castrejon-pita@ucl.ac.uk

‡ r.pita@ucl.ac.uk

adsorption [15]. However, bubble pressure tensiometers are usually expensive and less suitable for highly viscous fluids [16].

Viscosity is another key property that controls various aspects of fluid mechanics on the capillary scale, including jetting[17], spray dynamics[18], and liquid break-up [19]. In industrial environments, viscosity is often measured by vibrational viscometers and rheometers. Vibrational methods work by quantifying the viscous damping of shear acoustic waves through the liquid. These viscometers are fast, easy to operate, and provide reliable results for liquids in which viscosity remains constant regardless of shear; these liquids are commonly referred to as ‘Newtonian fluids’. A disadvantage of vibrometers is that they require large volumes of liquid, often in the 200 ml range. Liquids with shear-dependent viscosity, such as shear-thinning or thickening, and viscoelastics, require capillary and/or rotational rheometers [20]. These rheometers determine viscosity by applying a controlled shear stress, measuring the resulting flow response of the fluid. Unfortunately, rheometers are often both expensive and unsuitable for the fast-shear rates found in sprays and inkjet printing [21, 22].

Whilst effective, the traditional techniques described above form a segmented toolkit that lacks integration and are often incompatible with automation. In this work, we present an integrated, automation-friendly methodology, utilizing both supervised and unsupervised machine learning techniques, that can determine the surface tension, or the viscosity, or both, of Newtonian fluids from a single snapshot of a dripping drop. In our methods, the flow rate, the nozzle size, the density, and, if available, the viscosity or the surface tension are used as additional inputs.

In more detail, high-resolution and high-speed imaging experiments were conducted in this work to capture the last moments before the break-up of dripping droplets. From these images, droplet contours were extracted and used as key input features to supervised learning models. Various models are then trained to predict physical parameters, such as the viscosity and surface tension, directly from the image data. In addition, models are trained to predict the break-up shape of liquids given their material properties and flow rate. Unsupervised clustering algorithms are additionally employed to discover latent structures within the dataset, enabling the identification of distinct droplet behaviours, or quality modes, without requiring predefined labels. ML methods require sufficient and representative datasets, along with well-defined input features and target outputs; here, the training is carried out directly from experimental data, taken under a large variety of conditions, ensuring that the learned models capture the intrinsic complexity of wide laboratory conditions. This dual (supervised plus unsupervised) approach not only offers a fast and automated alternative to conventional rheometry and tensiometry but also reveals interpretable morphological patterns linked to fluid properties and experi-

mental conditions. Ultimately, our integration of physics-informed imaging (based on our hypothesis) and machine learning offers a scalable and generalizable pathway for data-driven fluid diagnostics.

II. BACKGROUND

A. Liquid breakup

For over a century, the break-up of liquid jets and filaments has been at the forefront of fluid mechanics, given its relevance to a myriad of processes ranging from lava ejection and fragmentation to inkjet printing [23, 24]. This phenomenon, while seemingly simple, involves complex dynamics where a liquid thins, or necks, rapidly until pinch-off, evolving through dramatic interfacial changes, all within a few microseconds [25]. Indeed, the point of break-up is a finite-time singularity and its description requires both scaling arguments and high-resolution experiments and modelling to resolve features that arise in its vicinity. A comprehensive theoretical framework has classified the routes to break-up into various canonical regimes depending on the relative importance of inertia, capillarity, and viscosity [25]. In the inviscid regime, where inertia balances surface tension, the thinning of a liquid neck follows the power law $h_{\min} \sim (t_b - t)^{2/3}$, where h_{\min} is the minimum neck radius, t_b is the break-up time and t is time. Interestingly, liquid break-up under this regime shows self-similarity where, regardless of the flow conditions, the liquid interface near pinch-off converges toward a unique shape, offering a powerful criterion for identifying inviscid liquids[26, 27]. This regime is often observed in low-viscosity fluids such as water or ethanol, when surrounded by a negligible ambient environment[28, 29].

In most other liquids, both viscosity and inertia play a dominant role. In fact, when viscous forces dominate, the thinning is characterized by a linear scaling, i.e. $h_{\min} = 0.0709 \left(\frac{\sigma}{\mu}\right) (t_b - t)$, where σ is surface tension and μ is the viscosity[30]. In contrast, in cases where all three forces, i.e. capillary, viscous, and inertial, play a role in the dynamics, the viscous-inertial regime leads to the universal scaling $h_{\min} = 0.0304 \left(\frac{\sigma}{\mu}\right) (t_b - t)$ [31]. A further fourth regime exists where the surrounding media viscosity, often another liquid, dictates the thinning and pinch-off dynamics[32]. It is worth noting that, on the route to break-up, the neck dynamics transition between these regimes based on the local importance of inertia, viscosity and surface tension effects[19]. The thinning regimes, and their transitions, are parametrized by two dimensionless parameters, the Reynolds ($Re = \frac{\rho Q}{\mu D}$), and the Ohnesorge ($Oh = \frac{\mu}{\sqrt{\rho \sigma D}}$) numbers, where Q is the volumetric flow rate, ρ is the liquid density, and D is a characteristic length (often the nozzle size or the neck diameter). In fact, the transitional behavior has been found to

consist of multiple intermediate transient regimes, which are highly sensitive to the liquid and flow properties. In other words, in their route to break-up, two liquids of similar characteristics can have a very different thinning transitional behavior [19]. Thus, the profile of a liquid neck near, or at, break-up is a repository of fluid dynamics information, reflecting the transitional competition of fluid properties and the flow at the neck. Complementary works have demonstrated that the break-up of liquid filaments, and the transition from dripping to jetting, are also ruled by the Reynolds and Ohnesorge numbers and by the filament length to diameter aspect ratio[33, 34]. A further dimensionless parameter, in addition to Re and Oh , the Bond number, $Bo = \frac{\Delta\rho g D_d^2}{\sigma}$, has been used to parametrize dripping from jetting, where D_d denotes the droplet diameter after break-up. These past findings support our hypothesis that the route to break-up is unique for each liquid and thus the resulting shape at the time of pinch-off is unique. Under this hypothesis, we have created a large database of images showing the last moment before break-up of fully characterized dripping droplets, to train ML models and predict liquid properties.

B. Machine learning

Machine learning (ML) is a branch of computer modeling that learns patterns from large amounts of data and makes predictions, or decisions, without prior knowledge beyond what it has learned from this data. In recent years, ML has been applied across various physics topics, including fluid dynamics[35–37], droplet physics [38–42], soft matter [43, 44], and materials science [45]. These studies highlight the potential of ML as a tool to complement traditional experimental and theoretical approaches in science. Specifically, supervised learning trains models on labelled datasets (data that has been manually classified or characterised), mapping inputs to known outputs, which is particularly effective for prediction tasks. In contrast, unsupervised learning operates on unlabelled data to identify hidden patterns or underlying structures, i.e. clusters. Both strategies offer valuable means of extracting knowledge from complex experimental observations. In addition, recent advances in computer vision[46] provide powerful tools for analysing image-based experimental data [47], which are highly relevant for the study of droplet dynamics and pinch-off processes where high-speed imaging is often used in conjunction with image analysis to extract information from images[19].

C. ML Applications to Droplet Dynamics

ML methods have been applied to various systems involving droplet formation, examples of these are on direct inkjet writing[48], droplet impact, spreading and bouncing on nanostructure substrates[49], spreading on various

materials [50], and droplet splashing [51]. Considering first the forward-prediction paradigm, in which ML models predict droplet behaviour from known material and operating conditions, Kim et al.[52] trained supervised regressors to predict the jetting behaviour of viscoelastic inks from rheological and drive parameters, with later work [53] using reinforcement learning to optimise actuation waveforms, dynamically improving jet stability without an explicit physical model. Additionally, Chen et al.[39] employed supervised learning to predict the optimum printable biomaterial formulations for direct ink writing, and Li et al.[41] developed a multi-parameter droplet optimisation model including flow and material parameters. Turning to image-based studies, Kratz and Kierfeld [40] introduced an image-based ML approach for pendant-drop tensiometry, demonstrating that the contour of a static droplet can be used to infer surface tension with the method restricted to steady pendant configurations. Pierzyna et al. [51] developed a data-driven model for the splashing thresholds and Au-Yeung et al. [49] developed a method to predict the maximum spreading and impact morphology of droplets on nanostructured surfaces.

In summary, previous works have predominantly used ML to control, or classify, droplet behaviour given known physical inputs. In contrast, the present work uses supervised learning to tackle the inverse problem of inferring fluid properties directly from droplet morphology, in addition, we use unsupervised learning to gain insight into the underlying physics of this process.

III. EXPERIMENTAL METHODOLOGY

In our experiments, dripping droplets were produced by pushing liquid, at a controlled flow rate, through long cylindrical nozzles. The flow rate was controlled by a KDS Gemini 88 Plus Dual Rate syringe pump, through Hamilton glass syringes (models 1750, 1001, and 1005; with nominal volumes of 0.5, 1.0 and 5.0 ml, respectively). Polyurethane tubing, of 6.0 mm diameter, connected the syringes to the nozzles by luer adaptors. The following flow rates were used: 100, 250, 500, 750, 1,000, 1,250, 1,500, 1,750, and 2,000 $\mu\text{l}/\text{min}$. The actual maximum flow rate per liquid was limited by the fluid viscosity, e.g. the maximum flow rate achieved for pure glycerine was $Q = 1,000 \mu\text{l}/\text{min}$. Six different nozzles were used in our experiments, with internal diameters of 0.10, 0.25, 0.83, 1.37, 1.79, and 2.38 mm. Prior to data acquisition, the liquid delivery system was carefully primed to minimise air entrapment. During experiments, the pump imposed a constant volumetric flow rate, producing a pendant drop that grew under gravity, underwent necking, and pinched off. The complete process, from necking to detachment, was recorded for subsequent frame-by-frame (visual) analysis to identify the frame nearest break-up.

Drop formation and pinch-off were recorded using the

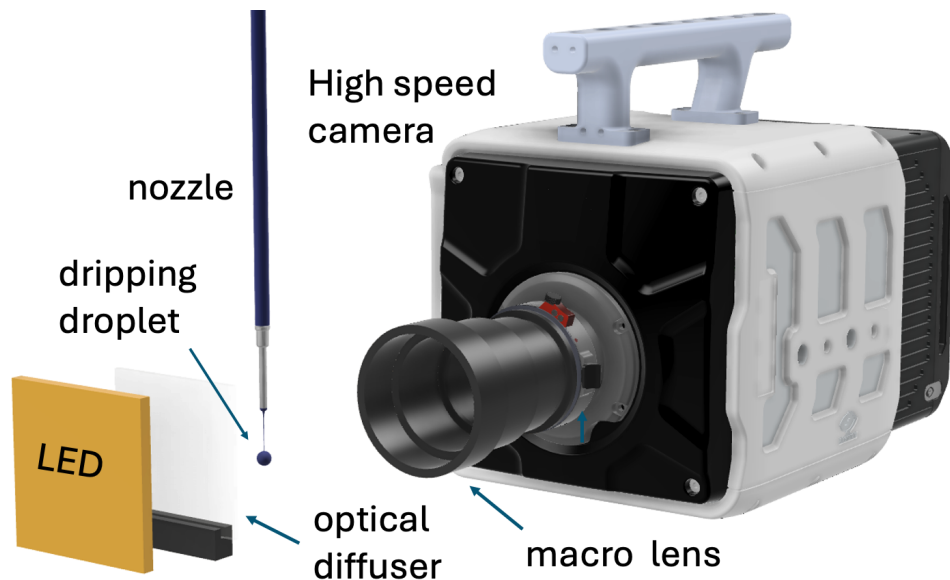


FIG. 1: Experimental setup used to capture the necking and break-up dynamics during droplet dripping. The system is a simple shadowgraph, where visualisation was carried out through a macro lens and a diffused light source.

back-lit, side-view, high-speed imaging system illustrated in Fig. 1. The setup consists of a high-speed camera (Phantom, TMX-5010), an off-the-shelf macro lens (Tamron macro), a vertical nozzle for gravity-driven dripping, a 500 Watt LED light, and an optical diffuser. The camera–lens axis was aligned orthogonally to the nozzle to obtain the side view. The diffuser is used to produce a uniform background and high-contrast images; some examples are seen in Figures 2. Images were acquired at a spatial resolution of $1,280 \times 800$ pixels, at a frame rate of $50,000 \text{ frames s}^{-1}$ and at an exposure time of $19 \mu\text{s}$. The optical resolution is in the range of 112 to 116 pixels/mm. This configuration provided sufficient temporal and spatial resolution to easily identify and capture the entire necking and pinch-off dynamics for all the conditions explored in this work.

A. Liquid materials and characterisation

All the liquids used in our experiments are well-known Newtonians, and are listed in Table I. They consist of aqueous solutions of glycerin and ethanol, pure methanol and silicon oils. Deionized water was sourced locally, from a IQ 7000 Milli-Q purification system (at $18.2 \text{ M}\Omega\cdot\text{cm}$ and 2.3 ppb TOC). (Pure) ethanol (TWL00000010683) and methanol (TWL0000001064) were obtained from Fisher Scientific, and glycerin was sourced from UK ONYX Ingredients (99.9 % pure). Silicone oils were acquired from Sigma Aldrich; these are 5 cSt (317667), 50 cSt (378356), and 1000 cSt (378399). The 2 cSt and 350 cSt silicone oils were obtained from Azeils (PMX-200).

The physical properties, i.e. density, viscosity, and surface tension, of the test liquids were characterised

| Liquid | μ (mPa s) | ρ (kg/m^3) | σ (mN/m) |
|--------------------------|---------------|----------------------------|-----------------|
| Water | 1.0 | 1,000 | 72.0 |
| 90% water / 10% glycerin | 1.5 | 1,005 | 71.5 |
| 70% water / 30% glycerin | 2.8 | 1,033 | 69.2 |
| 50% water / 50% glycerin | 6.8 | 1,082 | 67.4 |
| 30% water / 70% glycerin | 32.9 | 1,156 | 65.8 |
| 10% water / 90% glycerin | 225.1 | 1,206 | 63.8 |
| Glycerin | 1,350.0 | 1,248 | 62.8 |
| 90% water / 10% ethanol | 1.4 | 951 | 50.4 |
| 70% water / 30% ethanol | 2.5 | 927 | 34.2 |
| 50% water / 50% ethanol | 2.5 | 886 | 28.6 |
| 10% water / 90% ethanol | 1.6 | 811 | 23.9 |
| Ethanol | 1.2 | 789 | 22.2 |
| Silicon oil (2 cSt) | 1.8 | 900 | 17.7 |
| Silicon oil (50 cSt) | 48.6 | 960 | 20.8 |
| Silicon oil (350 cSt) | 348.0 | 969 | 21.1 |
| Silicon oil (1000 cSt) | 996.4 | 970 | 21.2 |

TABLE I: Physical properties of the tested liquids at $T = 20.0 \pm 1.0 \text{ }^\circ\text{C}$. Values of viscosity μ , density ρ , and surface tension σ used in this work.

at (working) room temperature of $(21.0 \pm 1.0 \text{ Celsius})$. Density was determined gravimetrically by weighing a known volume of liquid using an analytical balance. Viscosity was measured on a rotational rheometer (Anton Paar MCR 102e) equipped with a cone–plate geometry at a constant shear rate of 50 s^{-1} . Each sample was measured twenty times with the mean value taken as the working viscosity; the typical error in the viscosity measurement is $\delta\mu_{true} = \pm 0.10 \text{ mPa s}$. For liquids of low and moderate viscosity ($\mu \lesssim 60 \text{ mPa s}$), the surface tension was evaluated via the maximum bubble pressure method using a SITA pro line T15 tensiometer at bubble lifetimes from 1.0 s to 15.0 s. Within this range, surface tension

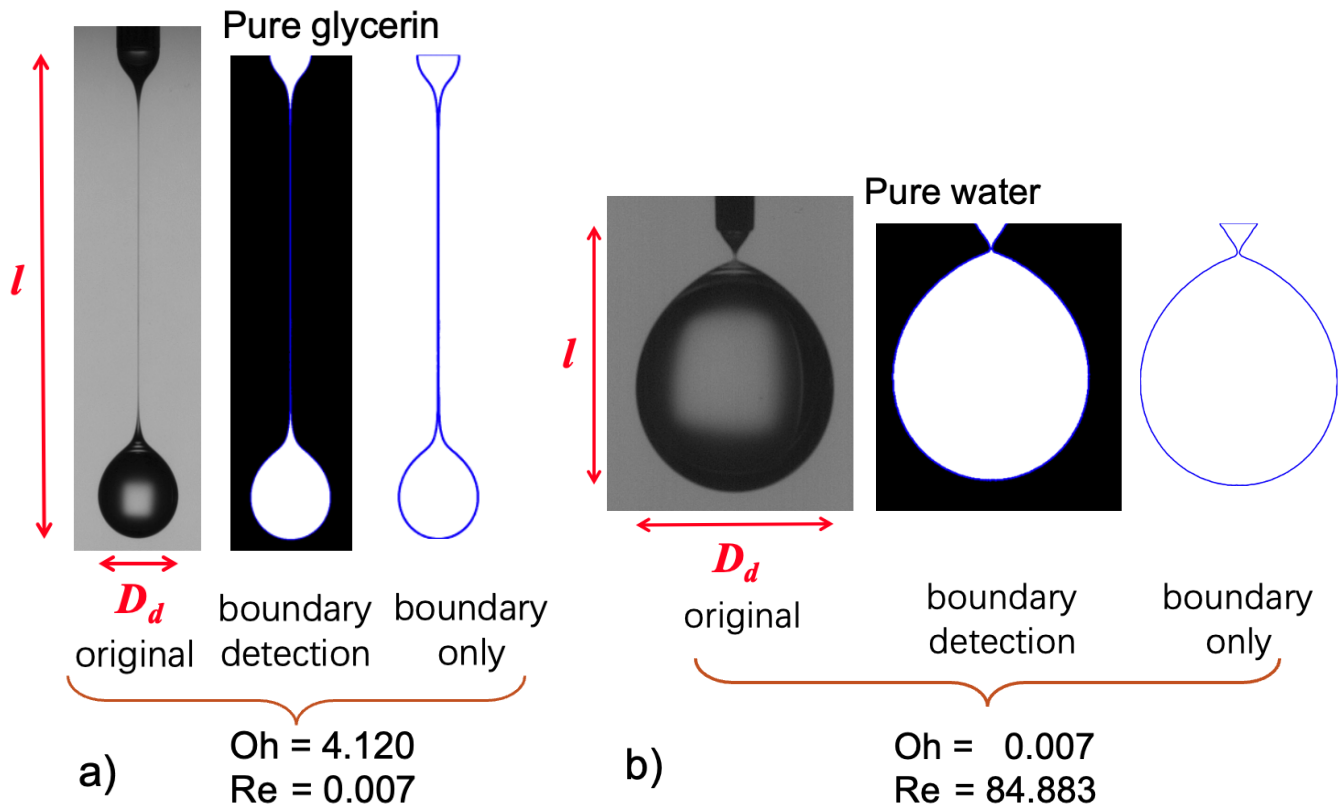


FIG. 2: Examples of the image-processing pipeline. The left panel shows the droplet at breakup, the middle panel shows the binary segmentation, and the right panel shows the extracted interface silhouette.

was found to be independent of surface age, with a standard error of $\delta\sigma_{true} = \pm 0.2$ mN/m. As noted in the introduction, bubble-pressure tensiometers are known to provide unreliable readings for highly viscous liquids due to viscous and hydrodynamic effects [16, 54]. Accordingly, for glycerin and water mixtures of a concentration ≥ 80 wt% glycerin, and for 350 cSt and 1000 cSt silicone oils, surface tension values were taken from the manufacturers' data-sheets. The resulting liquid property data is presented in Table I; we note that viscosity values span more than three orders of magnitude while surface tension triples in value. The domain of our data, parametrized in terms of Re and Oh , can be found in Fig. 3a. As can be seen there, our conditions cover four orders of magnitude in the Ohnesorge number and five in Reynolds, and include simple dripping, and jetting as defined in previous works [33].

B. Image Analysis

High-speed images were visually analysed to identify the nearest snapshot before break-up; this was done for each experiment. We carried out 840 conditions/experiments, each producing an image (snapshot) showing the break-up of the droplet. Each image was processed by custom MATLAB code to obtain the droplet

profile and its contour. The code works by first subtracting a pre-recorded background (image without a droplet, just the background) from the droplet snapshot to enhance the interfacial contrast. The code then employs a global threshold function (Otsu's method) to obtain a binary image [55]. This is followed by steps to remove image artefacts and holes. The largest connected region in the binary image is then identified as the droplet, and its exterior boundary is extracted as the raw contour. Finally, the boundary is smoothed and resampled uniformly. The needle outer diameter was used as size reference. Using this calibration, lengths, such as the droplet diameter D_d at pinch-off, could be calculated and recorded for each experiment for further analysis. Figure 2 illustrates some of the steps of the image analysis, and the droplet shape at the point of break-up, for: a) pure glycerin; and b) water. These boundary-only silhouettes constitute the sole image inputs for our computational methods.

IV. MACHINE LEARNING METHODOLOGY

Supervised and unsupervised machine learning techniques were employed for the data-driven prediction of liquid properties and droplet shapes. The supervised methods aim to either predict fluid properties based on physical inputs and latent shape features, or to recon-

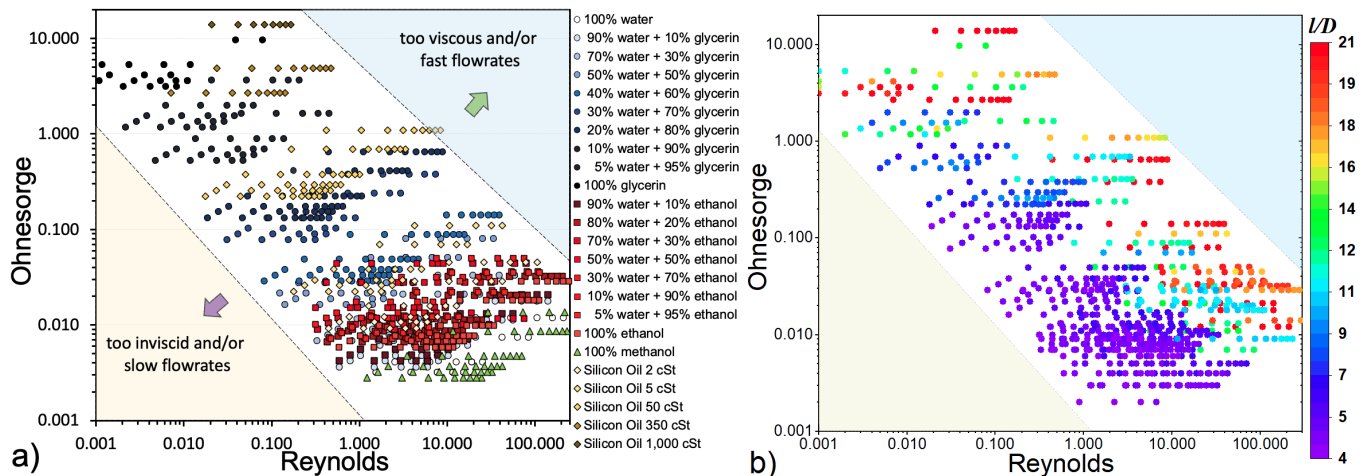


FIG. 3: Data domains in terms of the Reynolds and Ohnesorge numbers. a) Parametric space of fluid properties and flow characteristics in terms of the liquid type and formulation; most liquids correspond to aqueous solutions of ethanol and glycerin. b) Parametric space in terms of the dripping length to nozzle inner diameter ratio (L/D); as seen, the ratio is not a simple function of Oh and Re as many conditions lead to the same aspect ratio.

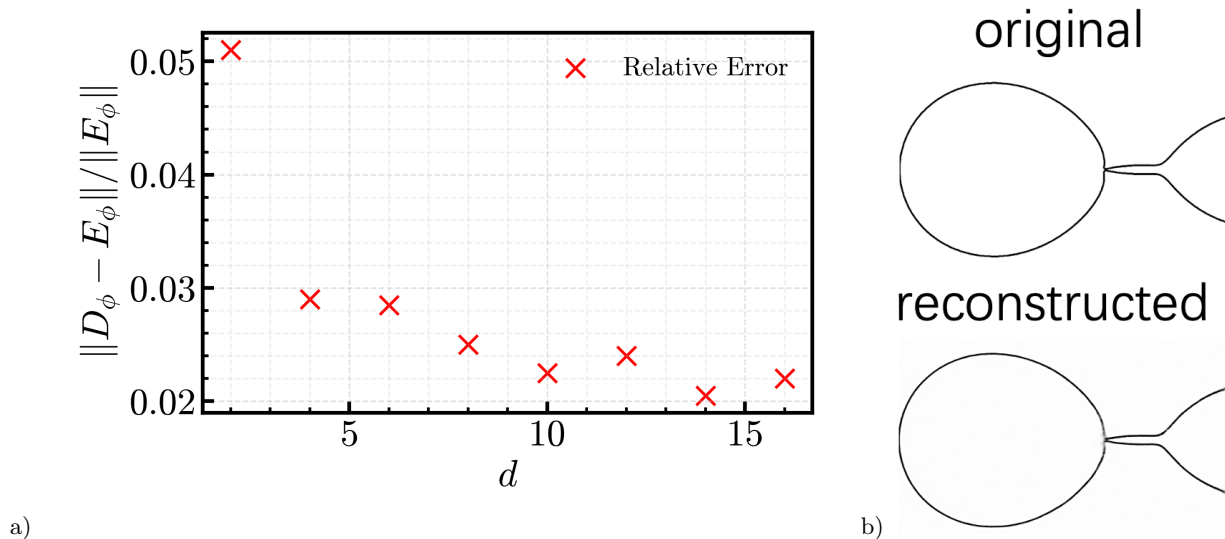


FIG. 4: Autoencoder error analysis : (a) Relative reconstruction error $\|D_\phi - E_\phi\| / \|E_\phi\|$ on the validation set versus the latent dimension d of the shape vector ($z \in \mathbb{R}^d$). As seen, the minimum error is found at $d = 14$, which is the value used in our models. (b) Qualitative comparison of a representative boundary: ground truth (*original*) vs. autoencoder output (*reconstructed*). Here, $Re = 7.943$ and $Oh = 0.004$ (90% water + 10% glycerin).

struct droplet shapes directly from physical parameters. In contrast, the unsupervised method focuses on identifying intrinsic groupings, i.e. clusters, of droplet characteristics based on experimental conditions and shape features.

A common foundation across both approaches is the use of a Convolutional Neural Network Autoencoder (CNN-AE) [46] to extract low-dimensional representations of the droplet snapshots, in the form of a latent shape vector \mathbf{z} . The structure of the autoencoder can be found in Table II in Appendix A. The primary motivation for employing a CNN is its ability to filter and

de-noise raw image data while reducing the input dimension. These features are then used as model inputs in the supervised learning tasks, or as clustering coordinates in the unsupervised learning analyses. Our dataset is constructed from the droplet boundary-only images previously described. We note the experimental images were obtained as high-resolution monochromes, but they were neither square nor of the resolution required. Consequently, to ensure consistent input sizes for the autoencoder, we padded the original images with a white background to transform them into square images of a 875×875 ($x \in \mathbb{R}^{875 \times 875}$) size; this padding

preserves the original resolution and aspect ratio of the droplet shapes without any downsampling or interpolation. CNNs require that all images within a batch share the same spatial dimensions; padding was therefore applied to obtain square inputs, standardizing image size and avoiding distortions caused by rescaling.

From our dataset of 840 samples we randomly selected 600 samples for training, 120 samples for validation, and 120 samples for the testing the autoencoder and the other methods. At each step, these groups of samples remained isolated from each other to avoid data leakage. The network was trained using the Adam optimizer [56] with a learning rate of 2.5×10^{-4} . An early stopping criterion was applied: if the validation loss did not decrease for 30 consecutive epochs, training was terminated. Under these conditions, the training converged after 140 epochs with a batch size of 32. Loss curves for the autoencoder are provided in Fig.11 in Appendix A.

It should be noted that the data used for validation are not the data used for final, out of sample testing; the test loss is only evaluated once training is completed and provides an unbiased measure of the final model performance. A learning rate scheduler reduces the learning rate by a factor of 0.5 after a quarter of the training epochs. To improve generalization, random Gaussian noise with a standard deviation of 0.02 is added to the input images during training. The model uses binary cross-entropy (BCE) loss, as the output is normalized. Mathematically, the autoencoder consists of an encoder E_θ and decoder D_ϕ , parameterized by θ and ϕ , respectively. Given an input image x , the BCE reconstruction loss is defined as

$$\mathcal{L}_{\text{BCE}}(x, D_\phi(E_\theta(x))) = -\frac{1}{N} \sum_{i=1}^N \left[x_i \log(D_\phi(E_\theta(x))_i) + (1 - x_i) \log(1 - D_\phi(E_\theta(x))_i) \right].$$

where x is the ground truth image, $D_\phi(E_\theta(x))$ is the reconstructed image, both with pixel values in $[0, 1]$, and N is the total number of pixels. This loss encourages the model to accurately predict pixel intensities in the reconstructed image [57]. The relative reconstruction error was computed as

$$\text{RE}(x, D_\phi(E_\theta(x))) = \frac{\|x - D_\phi(E_\theta(x))\|_2}{\|x\|_2}.$$

The validation set was then used to evaluate the reconstruction performance of the autoencoder. Figure 4a shows the relative reconstruction error as a function of the latent dimension. Our results indicate that the relative error decreases rapidly as the latent dimension d (the length of vector \mathbf{z}) increases, and plateaus around $d = 14$, indicating that adding more dimensions does not improve accuracy. Consequently, in our methods, we set the autoencoder to produce a vector \mathbf{z} of size $d = 14$.

We note that we have found a low-dimensional representation with a dimension in $\mathcal{O}(10^1)$, starting from an input dimension of $\mathcal{O}(10^5)$; thus a reduction of four orders of magnitude is achieved. A representative reconstruction example is found in Fig. 4b, contrasting the original contour and the reconstruction (with $d = 14$), and demonstrating that the autoencoder effectively captures the overall droplet geometry.

A. Predicting liquid properties & droplet shape with supervised learning

In this section, we describe the supervised models used to infer either one or two fluid properties (viscosity and/or surface tension) from images, or to predict the droplet shape from a set of known physical parameters. All supervised learning models were implemented using two types of algorithms: multilayer perceptron (MLP) and gradient boosting decision trees (XGBoost) [58], which differ in their learning paradigms. The four XGBoost tasks, or models, considered are summarized in Figure 5, and details the MLP model are found in in Appendix B. Neural networks learn smooth continuous mappings, while XGBoost captures nonlinear feature interactions through ensembles of decision trees—allowing a complementary comparison between deep and tree-based methods. Models 1–3 combine the autoencoder latent vector \mathbf{z} with physical parameters (nozzle diameter, flow rate, density, viscosity, and surface tension) to predict fluid properties. Model 4 performs the inverse mapping, predicting droplet shape from the same physical parameters, thereby establishing a bidirectional link between geometry and material behaviour. In addition, the same train, validation, and test split as used for the autoencoder was used here, with the same strict separation of these sets, in order to prevent data leakage. Each model was trained using the Adam optimizer with an initial learning rate of 10^{-3} and the mean-squared-error (MSE) loss function,

$$\mathcal{L}_{\text{MSE}} = \frac{1}{N} \sum_{i=1}^N \|\hat{y}_i - y_i\|_2^2.$$

where N denotes the number of samples in a batch. For Models 1–3, the output values were log-transformed during training to improve numerical stability. A batch size of 32 was employed, and a StepLR scheduler was applied with a step size of 100 epochs and a decay factor of 0.8. Early stopping with a patience of 100 epochs was applied based on validation loss, and the model weights corresponding to the lowest validation loss were restored for testing. For targets with large dynamic range (e.g., viscosity), the outputs were log-transformed during training to improve numerical stability, and then mapped back to the physical scale for evaluation.

Models 1 and 2 are formulated as single-task regressors. In Model 1, the inputs consist of the droplet shape latent

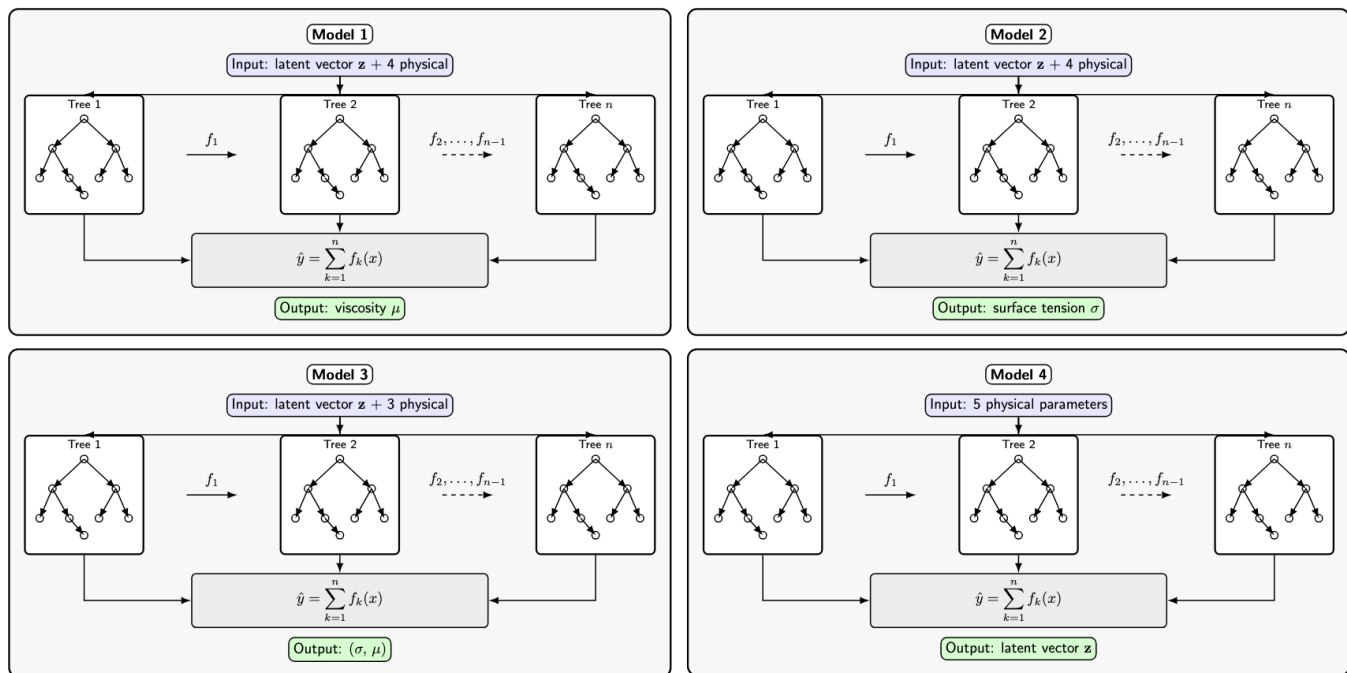


FIG. 5: Supervised learning framework (XGBoost). Model inputs consist of physical parameters and, when required, the 14-dimensional latent droplet representation. The models predict viscosity (Model 1), surface tension (Model 2), viscosity and surface tension (Model 3), or the 14-dimensional shape descriptor (Model 4).

vector obtained from the CNN encoder, together with the density, diameter, flow rate and the surface tension; the network is trained to predict the viscosity μ . Model 2 receives the same latent vector, plus density, diameter, flow rate, and the viscosity μ , to predict the surface tension σ . These two models served as baselines, inferring one unknown physical property of the example given the droplet shape (via the encoder representation) and the known other physical properties. Model 3 extends this approach to a multi-task setting. Here, the inputs are only the latent shape vector and the control parameters of density, nozzle size and flow rate, and the network simultaneously outputs both viscosity μ and surface tension σ . This design allows the model to learn a shared network structure for the two correlated fluid properties, and provides a more realistic scenario in which neither property is known a priori. Together, Models 1 to 3 provide a progressive comparison between single-task and multi-task learning for fluid property prediction. The performance of the models was assessed by the coefficient of determination R^2 , defined as

$$R^2 = 1 - \frac{\sum_{i=1}^n (y_i - \hat{y}_i)^2}{\sum_{i=1}^n (y_i - \bar{y})^2},$$

where y_i denotes the true (experimentally obtained) values, \hat{y}_i the (ML-obtained) predicted values, and \bar{y} the mean of the true values.

Model 4 takes a different approach by requiring only physical parameters as input to regress the latent vec-

tor. The model is thus trained to reconstruct the droplet image. Model 4 directly predicts normalized latent vectors, which are subsequently denormalized and decoded into droplet boundaries. For Model 4, a CNN was implemented to learn compact representations of droplet shapes that directly map the high-dimensional grayscale images to a low-dimensional representation. Unlike classification models, or supervised regressors, this autoencoder was trained in a self-supervised manner relying solely on raw pixel values of the droplet images. The encoder network consists of six convolutional layers with increasing channel depth (32, 64, 128, 256, 256, 256), followed by a flattening operation and a fully connected layer that outputs a latent vector $z \in \mathbb{R}^d$. The layer configuration was chosen to balance model expressiveness and computational cost. The decoder performs the inverse operation: it projects the latent vector back into a high-dimensional feature map, and then uses transposed convolutions to reconstruct the original image of size 875×875 . The output is a grayscale image with pixel intensities normalized between 0 and 1.

B. Uncovering natural groupings in droplet behaviour with unsupervised learning

In addition, we have employed unsupervised learning to directly uncover naturally occurring group behaviour in droplet dynamics from the observed shapes and imposed flow conditions, without requiring prior knowledge

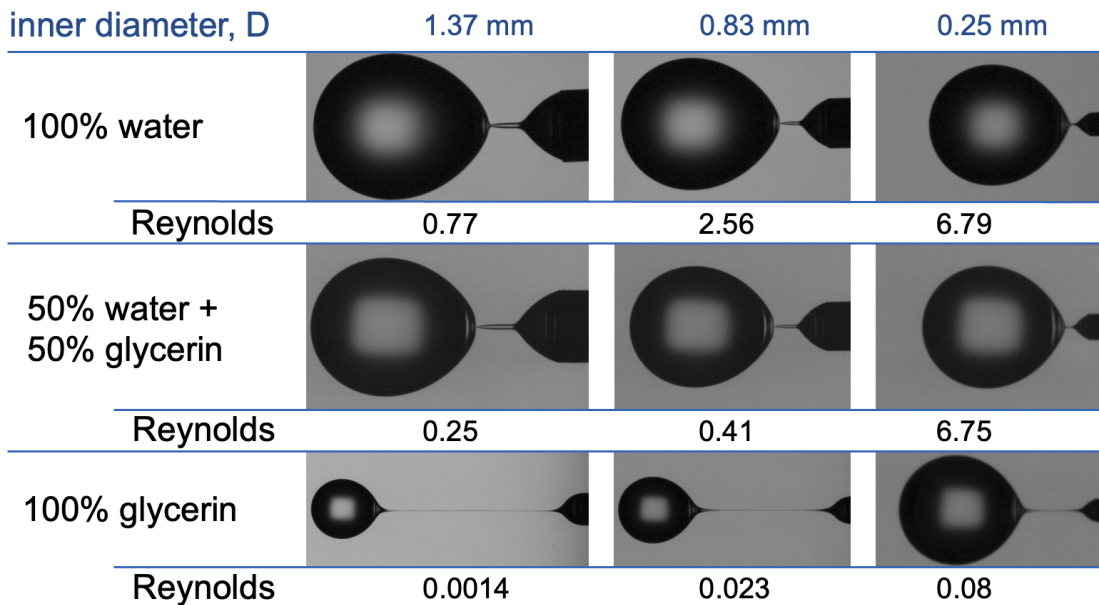


FIG. 6: Examples of breaking up droplets at various conditions of Reynolds numbers for different liquids. As expected, pure water shows self-similarity near the pinch-off point and pure glycerin presents long filaments that break-up from the middle. Snapshots of pure glycerin are not to scale.

of the underlying fluid properties.

This work is motivated by experimental scenarios in which viscosity or surface tension are not readily measurable, yet droplet morphology and control parameters are accessible, e.g. in systems where liquid volumes are too small. Specifically, we extracted low-dimensional latent features $z \in \mathbb{R}^{14}$ from the encoder, with the latent dimension $d = 14$ adopted from Section IV, where it was identified as the optimal representation size. These latent features were combined with two directly controlled experimental parameters, nozzle inner diameter and flow rate, for clustering. Notably, we deliberately excluded any information related to the fluid properties, as these quantities are often difficult to measure in practice. We applied both K-Means and Gaussian Mixture Models (GMM) with cluster numbers K . To identify optimal settings, we systematically tested $K \in \{2, 7\}$. The choice of the upper bound $K = 7$ reflects a practical consideration: while larger values of K might further partition the data, excessively fine-grained clustering may produce groups which lack clear physical interpretation in the context of droplet dynamics. Thus, restricting K to moderate values ensures a balance between capturing heterogeneity in the dataset and maintaining physically meaningful cluster assignments.

In order to assess clustering quality, we employed two complementary metrics, the Silhouette Score [59] and the Davies-Bouldin Index (DBI) [60]. The Silhouette Score quantifies how well a sample fits within its assigned cluster compared to the nearest alternative cluster. For a

data point z_i , the score is defined as

$$s(z_i) = \frac{b(z_i) - a(z_i)}{\max\{a(z_i), b(z_i)\}},$$

where $a(z_i)$ denotes the mean distance from z_i to other points in the same cluster, and $b(z_i)$ is the mean distance to points in the nearest different cluster. A higher Silhouette Score, approaching 1, indicates that the clusters are well-separated and compact. The DBI, on the other hand, measures the average similarity between each cluster and its most similar counterpart, defined as

$$DBI = \frac{1}{K} \sum_{i=1}^K \max_{j \neq i} \left(\frac{s_i + s_j}{d_{ij}} \right),$$

where s_i is the average distance between points in cluster i and its centroid, and d_{ij} is the distance between the centroids of clusters i and j . Lower DBI values indicate better clustering performance, favoring compact and well-separated clusters. The algorithm settings for GMM and K-Means are provided in Appendix C, and the evaluation of the cluster number K is discussed in Appendix D.

V. EXPERIMENTAL OBSERVATIONS

Figure 6 presents examples of snapshots captured at the frame immediately prior to breakup. The images are organised by nozzle diameter D and the liquid composition. As can be seen, water (a near inviscid fluid) displays

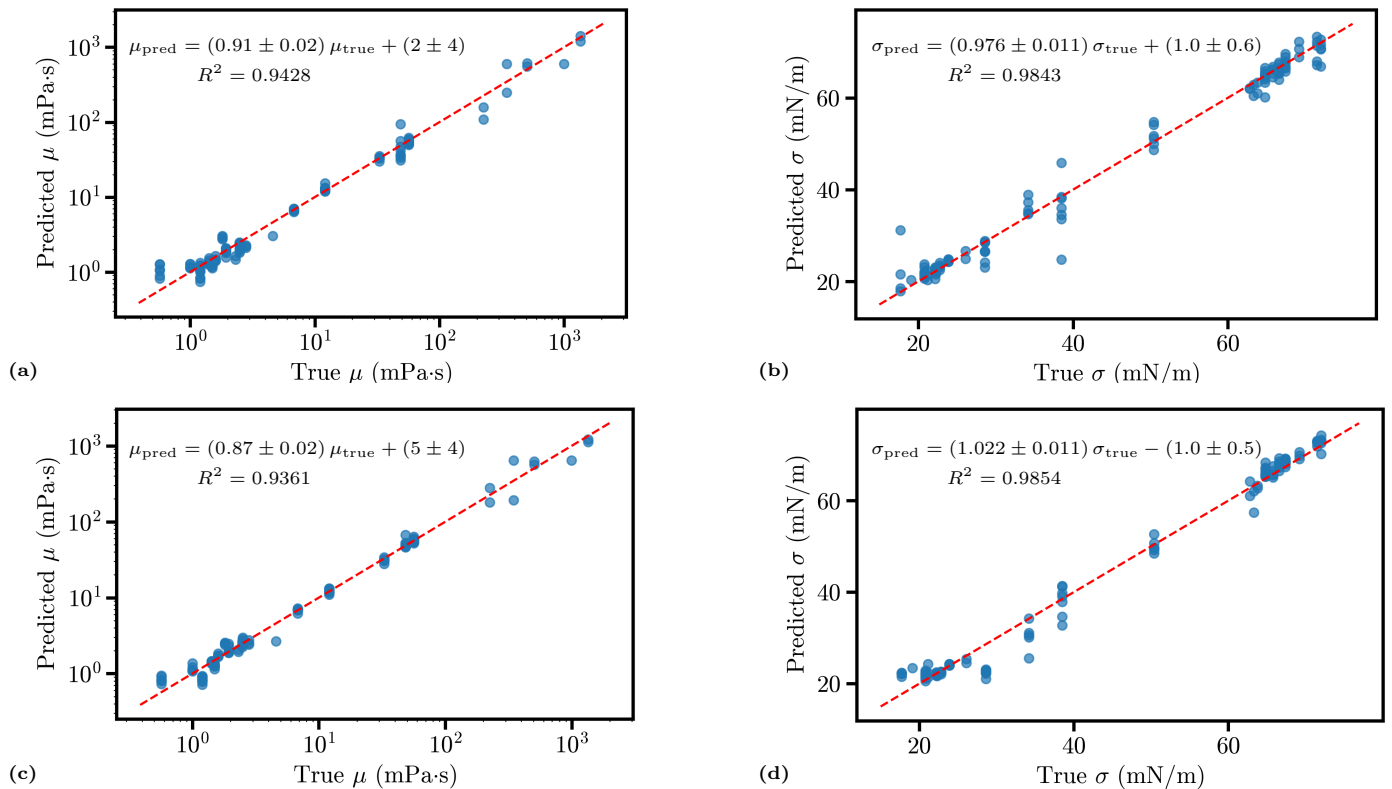


FIG. 7: Predicted vs. true values on the test set for Models 1–3 (MLP). Model 1 (a) predicts viscosity, Model 2 (b) predicts surface tension, and Model 3 predicts both viscosity (c) and surface tension (d).

a characteristic sharp neck that previous works have confirmed takes a 18 degree angle. In contrast, the 50% mixture forms a longer, more gradually evolving neck, which indicates viscosity is playing a role in the dynamics. Interestingly, regardless of having very similar Reynolds numbers, pure water and 50% glycerin (with $D = 0.25$ mm) have visibly different shapes, with the glycerin solution having a larger bulb. Pure glycerin shows a slender, quasi-cylindrical long filament, that pinches off at the middle, consistent with a viscous-dominated dynamics. The Reynolds numbers listed beneath the panels increase as D decreases, e.g. for water $Re = 0.77 \rightarrow 2.56 \rightarrow 6.79$, and for glycerin $Re = 0.001 \rightarrow 0.023 \rightarrow 0.080$). As can be seen, increasing viscosity (decreasing Re) shifts the minimum neck radius upstream and increases the break-up length to nozzle diameter aspect ratio.

The parameter map in Figure 3a identifies different liquids within the Re - Oh plane. As expected, methanol is found at the lowest Oh values due to its low viscosity. In contrast, aqueous ethanols are found in the low- Oh , and moderate to high Re , region due to their low viscosities and surface tensions. Glycerin-water mixtures occupy intermediate Oh values across a wide range of Re , with pure glycerin, and high-viscosity silicone oils, situating at high Oh and low Re . The accessible domain of our setup is limited in the low left by very low viscosity and very slow flow rates, and in the upper right by

the maximum pumping pressure, which limits the flow rates. We argue that our domain of experimental conditions is sufficiently extensive as it includes very low viscosity liquids (methanol and water), intermediate viscosities (solutions) and very high viscous fluids (silicon oil and glycerin), and very low surface tension (silicon oils) and high surface tension liquids (water).

Figure 3b provides an alternative perspective by color-mapping the break-up length-to-nozzle diameter ratio L/D across the Re - Oh space. As noted in the Introduction, the L/D ratio has been used to determine whether a liquid filament will break up or not, and to distinguish dripping from jetting conditions [33, 34]. From our results (the colour redundancy in Figure 3b), various Re and Oh conditions lead to the same dimensionless break-up length; it is hence clear that the aspect ratio alone is insufficient to predict liquid properties, or a flow characteristic.

VI. MACHINE LEARNING RESULTS

A. Supervised learning results

The four supervised models provide complementary perspectives on the extent to which fluid properties and droplet geometries can be inferred from a combination

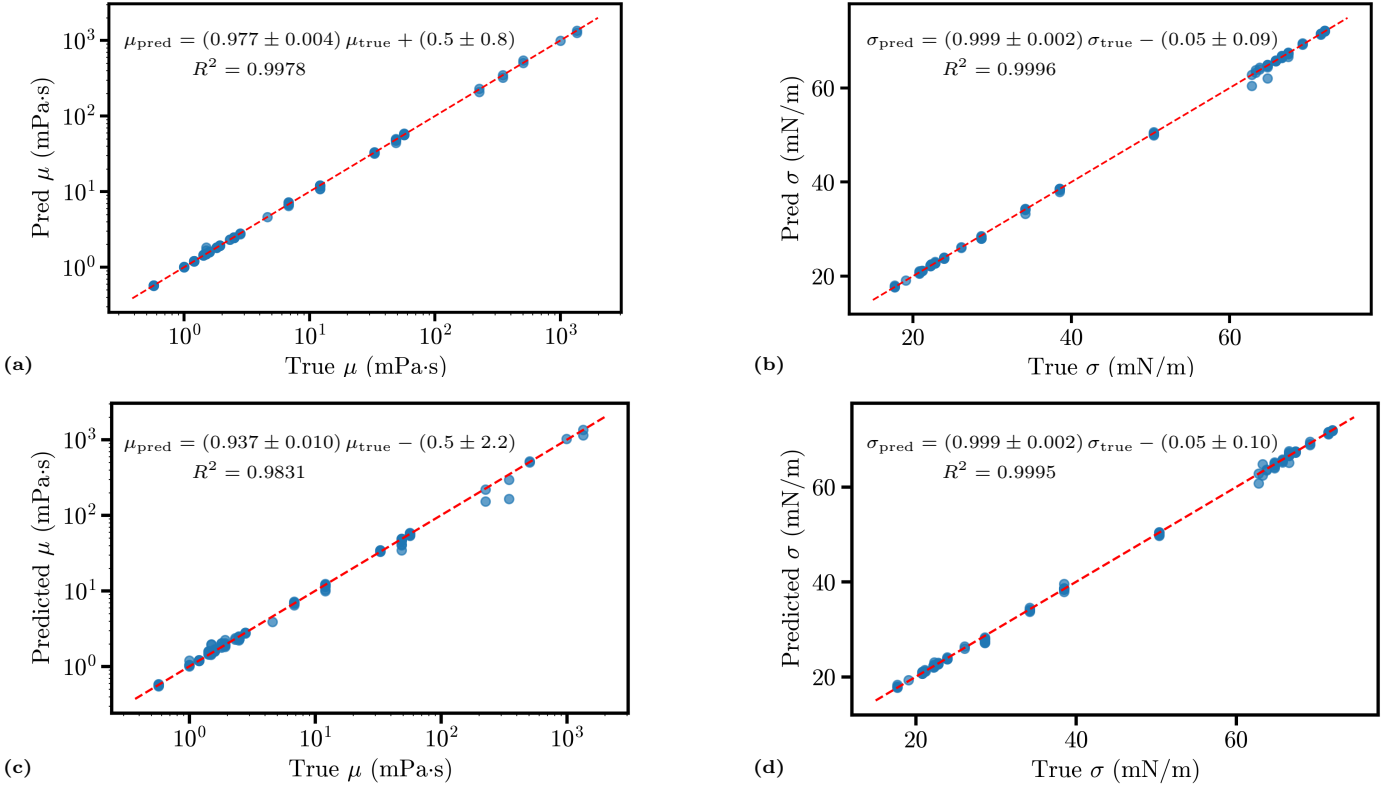


FIG. 8: Predicted vs. true values on the test set for Models 1–3 (XGBoost). Model 1 (a) predicts viscosity, Model 2 (b) predicts surface tension, and Model 3 predicts both viscosity (c) and surface tension (d).

of physical parameters and learned shape representations. We evaluated the predictive performance of all four supervised-learning models on the test set, using the coefficient of determination (R^2) between predicted and true values as the main metric.

Model 1, implemented as a multilayer perceptron (MLP), predicts the viscosity from the other liquid properties, the flow characteristics, and the image-derived shape features. Figure 7a uses a logarithmic scale and covers more than three orders of magnitude; we obtain $R^2 = 0.9428$. In contrast, with the same inputs, gradient boosting decision trees (XGBoost) reaches $R^2 = 0.9978$ (Fig. 8a), confirming that the viscosity signal is extremely well aligned with the latent geometry. We note that XGBoost is known to handle well small datasets.

Model 2 addresses the complementary task of predicting surface tension from the same inputs as Model 1, but with surface tension removed from the inputs and viscosity provided instead. The MLP attains $R^2 = 0.9843$ (Fig. 7b), while the XGBoost model slightly improves this to $R^2 = 0.9996$ (Fig. 8b), indicating that the latent vector indeed contains geometric markers that are controlled by capillarity.

Model 3 is the multitask setting, predicting both viscosity and surface tension together. Our MLP yields $R_\mu^2 = 0.9361$ for viscosity and $R_\sigma^2 = 0.9854$ for surface tension. The XGBoost version of the same task improves

the numbers to $R_\mu^2 = 0.9831$ and $R_\sigma^2 = 0.9995$ (Fig. 8c and 8d). Despite having to predict two parameters simultaneously, the multi-task setting maintains essentially the same fidelity as the single-task models.

Model 4 differs from the others in that it predicts the *shape* (the latent vector) directly from physical parameters, without any image as input. Using the MLP, we previously obtained $R^2 = 0.9145$ on the test set when comparing predicted latent vector. The XGBoost model reaches $R^2 = 0.9713$ in the normalized latent space. Because the decoder is a nonlinear map from latent coordinates to pixels, part of this advantage is smoothed out after decoding, but the high latent-space R^2 confirms that a large fraction of the image variability can be explained directly from the physical descriptors. Representative predictions are shown in Fig. 9a and Fig. 9b, we can see that both MLP and XGBoost models provide good prediction. Both models reproduce the global morphology reliably: the bulb radius, neck position, and overall aspect ratio match the ground truth. From the differences in the figures, it can be seen that MLP better maintained the continuity of the lines, but slightly underestimated the terminal bulbs, while XGBoost underestimated the thickness of the filament neck.

We noted that, across all four supervised tasks, both the MLPs and the XGBoost models consistently achieve test-set $R^2 > 0.9$, and in the viscosity case the boosted

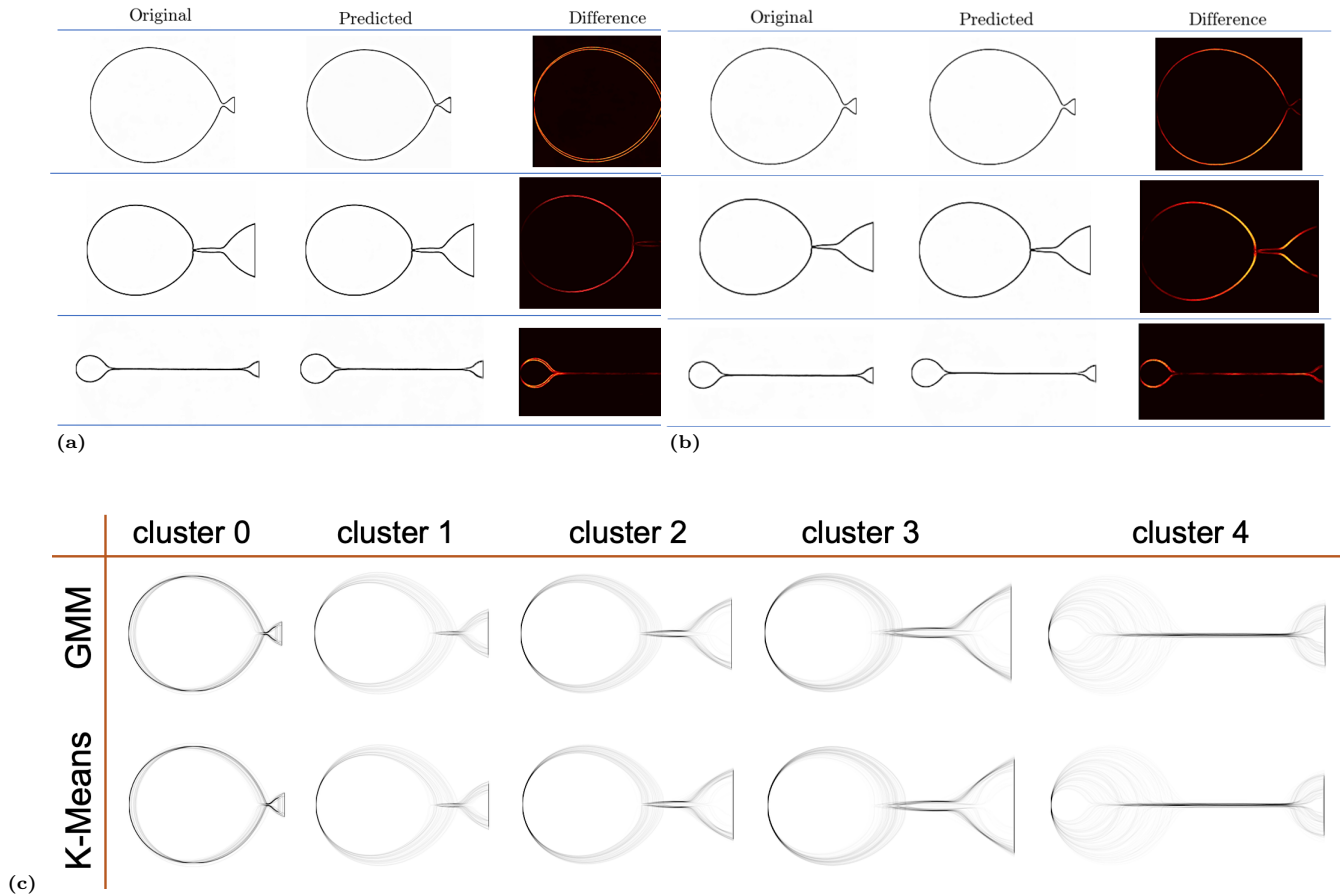


FIG. 9: Model 4 predictions: experimental vs. predicted droplet shapes for both (a) MLP and (b) XGBoost variants. (c) Unsupervised learning results: average droplet shapes discovered by GMM and *K*-Means clustering in latent space.

model is effectively at the noise floor ($R^2 \approx 0.998$). This compares favourably with prior work [38, 42]. Remarkably, the tree-based models (XGBoost) match or even slightly outperform the MLPs on several tasks. This is likely because the physical properties in our dataset, e.g. viscosity and surface tension, take only discrete values, determined by the limited categories of liquids used. While the MLP attempts to learn a smooth, continuous mapping, XGBoost is naturally better suited for capturing piecewise-constant relationships arising from such discrete labels. The performance of all 4 models show that once a good latent vector is available, even a relatively shallow ensemble of boosted trees can exploit it extremely well.

B. Unsupervised learning results

We employed unsupervised clustering on the feature representations extracted by the convolutional neural network to identify intrinsic groupings in the droplet dynamics, based on the droplet images in our validation dataset. From the behaviour of the Silhouette and DBI metrics across candidate values of K (see Appendix D),

we selected $K = 5$ for both K-Means and GMM, corresponding to a maximum Silhouette Score. In the case of the DBI, extending K beyond this value did not result in a large improvement, and, as previously noted, a smaller number of clusters is preferable for insight into the underlying physics.

We computed the average decoded shape of all droplets within a cluster to visualize the typical droplet morphology for that cluster. Figure 9c shows these mean shapes for the GMM and K-Means partitions. Both methods readily and consistently identify Cluster 4 as a bulb attached to a very long filament, and Cluster 0 as a wide and rounded bulb coming from a small-in-comparison nozzle (with no connecting filament). The other three clusters only differentiate in the relative size of the nozzle and its connecting filament. Cluster 1 consists of elongated droplets connected to a small nozzle through a short filament, Cluster 3 is a droplet connected, through a filament, to an equal-in-size nozzle, and Cluster 2 is a droplet connected to a intermediate-in-size filament and nozzle. The close agreement between the average shapes from the two methods confirms that both clustering approaches capture coherent and meaningful droplet shape features.

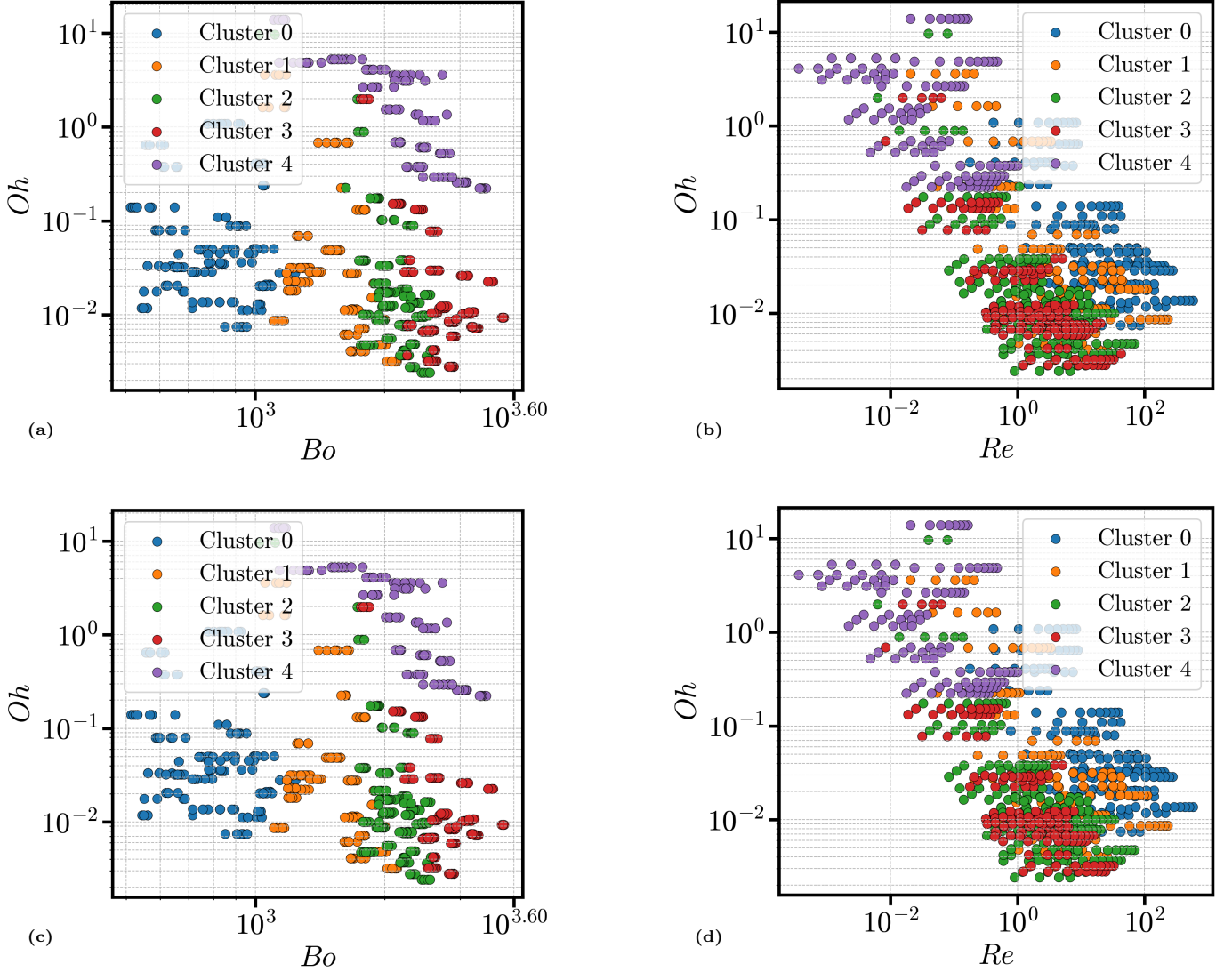


FIG. 10: Clustering of droplet breakup regimes in the Bo - Oh and Re - Oh parameter spaces. Panels (a) and (b) show K -means clustering, while panels (c) and (d) present the Gaussian mixture model (GMM) results.

A central question arising from the clustering is whether the unsupervised method effectively identifies, or differentiates, the underlying regimes and the various other factors influencing the dripping and break-up dynamics. Following previous works [25], that have classified the liquid break-up dynamics in terms of scaling arguments, Figure 10a and Figure 10c show the cluster data projected onto the log-log (Re, Oh) plane for GMM and K -Means. Importantly, some clusters are readily physically interpretable. Decreasing Oh indicates weakening viscous effects relative to inertial-capillary stresses, while increasing Re reflects stronger inertia at fixed viscosity. Both methods clearly separate Cluster 4 and Cluster 0. Cluster 4 lies predominantly in the upper-left quadrant (high Oh , low Re), consistent with viscous-damped pinch-off with limited necking and slow recoil, and visually associated with very long filaments. In contrast, Cluster 0 concentrates in the lower-right region (low Oh , high Re), characteristic of inertial-capillary breakup pro-

ducing small, nearly spherical droplets with weak viscous damping. Further analyses can be carried out by reflecting on the distribution of liquid formulations among the clusters, as summarized in the Table III and IV in Appendix E. A clear pattern emerges from these analyses: high viscosity fluids, such as glycerin-rich solutions and high cSt silicone oils, are consistently grouped into Cluster 4 by both GMM and K -Means. These samples correspond to the most elongated droplets, supported by the high ratios L_2/L_1 and the mean shapes shown in Figure 9c. In contrast, low-viscosity and low-surface-tension fluids are more frequently assigned to Cluster 0. These groups correspond to rounder, more stable droplets with minimal tailing.

Interestingly, Clusters 2 and 3 overlap in the low Re and low Oh quadrant, a region reserved for low viscosity liquids dripping at low flow rates. Furthermore, Cluster 1 is seen occupying the whole parametric space with no distinct regime, or liquid, or flow property in common.

Intermediate formulations such as ethanol-rich fluids are more diffusely distributed across Clusters 2, 3 and 4, suggesting transitional regimes. The clustering results also show strong consistency between GMM and K-Means for the same liquids; this alignment reinforces that the latent feature space captures essential morphological cues that reflect fluid properties—even though clustering is entirely unsupervised and image-driven.

The lack of a common denominator among data clusters 1, 2, and 3 suggests that a further factor, apart from the flow rate, the nozzle size, and the liquid characteristics, is playing a role in driving the dripping dynamics. Fortunately, dripping is well-known to be governed by a third dimensionless parameter, the Bond number [25]. Figure 10a and 10c show the data and clustering in the Bo – Oh space, where all five clusters are well separated, indicating distinct regimes governed by the relative importance of gravity (Bo) and viscosity (Oh). Clusters 0–3 occupy a narrow range of Oh but progressively shift toward larger Bo . This increase in Bo indicates that these clusters primarily reflect the gradual strengthening of gravitational forces relative to capillarity, while viscous effects remain comparatively constant. Cluster 0 corresponds to the capillary-dominated regime, where droplets are nearly spherical and detach quasi-statically. The gravitational effect strengthens among Clusters 1–3; even though they have comparable viscosity, the increasing gravitation elongates the filaments. In contrast, Cluster 4 deviates markedly from this Bo -driven sequence; it spans to much higher Oh values while maintaining moderate Bo , this corresponds to high viscous effects in which surface tension and gravity are both resisted by strong viscous damping.

As described in Section IV B, the clustering was performed on a feature vector that concatenates droplet-shape descriptors with the experimental settings (nozzle diameter and mean flow speed) and does not explicitly include fluid properties. The data separation in Re – Oh and Bo – Oh therefore suggests that these features implicitly encode the inertia–viscosity–gravity balance. Notably, the physical properties of the liquids were not input into the clustering. Thus the separation in Re – Oh and Bo – Oh space indicates that our method successfully uncovered the underlying physics linking the experimental settings to the observed droplets. The strong mapping between physical composition and cluster assignment provides further evidence that the unsupervised clusters are not only mathematically separable but also physically interpretable.

VII. UNCERTAINTY ANALYSIS

Associating standard errors with machine learning predictions is not a common practice (or nonexistent to the best of our knowledge). To address this issue, in this section, we propose a simple, yet formal, method to associate uncertainties to the predictions of the models. The

idea is simple, and follows the standard method of contrasting predicted and true values. Figures 7 and 8 show various predicted values plotted against known properties. As with any other method, we observe the prediction is not perfect, with the data showing some scatter around the known values. When presented in this form, the predicted and true (experimentally measured) values can be linked by a linear fit, with a regression analysis able to provide us with average and error values for the slope and intercept. In brief, predicted and true values form the function

$$\zeta_{predicted} = m\zeta_{true} + b, \quad (1)$$

where $\zeta_{predicted}$ is the predicted property, which in our case can be either the surface tension or the viscosity, ζ_{true} is the true (measured) value, m is the slope, and b is the value taken by the prediction at a condition where the true value is zero (or the point where the line crosses the y -axis). In a perfect scenario, m would take a value of one, and b the value of zero, i.e. every prediction matching the true value. However, our predictions are not perfect, m is not one and b is not zero. In fact, our true values are also not uncertainty-free as they were obtained experimentally, with error. Propagation of uncertainty theory tells us that the error on the prediction (Eq. 1) is given by

$$\delta\zeta_{predicted} = \sqrt{(\zeta_{true}\delta m)^2 + (m\delta\zeta_{true})^2 + \delta b^2}, \quad (2)$$

where $\delta\zeta_{predicted}$ is the error of the predicted value, $\delta\zeta_{true}$ is the experimental error of the true value, δm is the error of the slope, and δb is the error of the y -axis crossing. Combining Eqns. 1 and 2 we obtain

$$\delta\zeta_{predicted} = \sqrt{\left(\frac{\zeta_{predicted} - b}{m}\right)^2 (\delta m)^2 + (m\delta\zeta_{true})^2 + \delta b^2}. \quad (3)$$

Applying this relationship to, for example, our viscosity predictions from the MLP model 1, Figure 7a, we obtain that the error on the prediction is

$$\frac{\delta\mu_{predicted}^2}{(\text{mPa s})^2} = 5 \times 10^{-4} (\mu_{predicted} - 2)^2 + 16.$$

From the analysis, we observe that the largest source of error of the MLP model 1 comes from δb , and thus it is inaccurate at predicting very low viscosity values. At the opposite range, i.e. high viscosities $> \mathcal{O}(10^2)$ mPa s, the error on the MLP method only represents a single digit percentile.

In contrast, the error analysis applied to models 1 and 3, from XGBoost, e.g. Figures 8a and d, produce much more accurate results:

$$\frac{\delta\mu_{\text{predicted}}^2}{(\text{mPa s})^2} = 1.7 \times 10^{-5} (\mu_{\text{predicted}} - 0.5)^2 + 0.65;$$

$$\frac{\delta\sigma_{\text{predicted}}^2}{(\text{mN/m})^2} = 4 \times 10^{-6} (\sigma_{\text{predicted}} - 0.05)^2 + 0.05.$$

As observed, the XGBoost models predict, within a single digit percentile, viscosities in the range $> \mathcal{O}(10^1)$ mPa s, but miss zeroing very low viscosities by 0.8 mPa s. In contrast, we note $\delta\sigma_{\text{predicted}}$ never exceeds 2% of the mean value making the XGBoost models particularly good for predicting surface tension.

VIII. CONCLUSIONS

In this study, we have systematically analyzed the pinch-off dynamics of Newtonian liquids, including water, methanol, silicone oils, ethanol, and aqueous ethanol and glycerol–water mixtures, using high-speed imaging across 840 experimental conditions spanning $0.001 < Re < 200$ and $0.01 < Oh < 20$. The frame immediately preceding droplet break-up was captured to record the pendant drop shape at detachment. The contour of each droplet was extracted and standardized for subsequent machine learning analysis. Supervised regression models were used to predict viscosity and surface tension from these contours and known flow parameters. We further built an inverse model that predicts the pinch-off shape from physical inputs, and employed unsupervised clustering to reveal morphology–physics structure in the data. We thus have created a bidirectional, image-driven pipeline linking droplet geometry and material properties. On supervised tests, single-task model achieve $R^2 = 0.9428$ (MLP) and 0.9978 (XGBoost) for viscosity, and $R^2 = 0.9843$ (MLP) and 0.9996 (XGBoost). In the multi-task setting, we obtained $R^2 = 0.9361$ (MLP) and 0.9843 (XGBoost) for viscosity, and $R^2 = 0.9854$ (MLP) and 0.9995 (XGBoost) for surface tension. For the inverse mapping, the test-set coefficient of determination in latent space reaches $R^2 = 0.9843$ with XGBoost (MLP: 0.9145), which is significantly better than MLP model, indicating that tree-based model performs better than simple MLP in these cases. In addition, our analyses demonstrate the XGBoost models perform very well in terms of errors, with surface tension predictions achieving a maximum percentage error $< 2\%$. These results demonstrate that the instantaneous pinch-off profile encodes fluid properties with high fidelity, and that a compact latent representation can be robustly regressed from physical parameters. Unsupervised analyses on latent shape features identify five physically interpretable clusters. The clusters separate cleanly across the Re – Oh and Bo – Oh plane, indicating that the latent representation captures genuine fluid-mechanical differences. This

could provide a new insight on the classification of droplet flow regimes. Our uncertainty analysis demonstrates the models work particularly well for surface tension predictions and for high viscosities, having limited success for low viscosity liquids.

Previous studies have demonstrated that the simultaneous measurement of surface tension and viscosity is possible using specialized techniques [61], but most traditional characterization protocols rely on separate tensiometers and viscometers, which often demand substantial sample volumes [62] and/or are limited by their measurement range [16]. Our approach provides a single-step measurement of both surface tension and viscosity, alleviating the need for multiple instruments [63]. Our results demonstrate a generalizable route to rapid, multi-parameter characterization of liquids from a single pinch-off snapshot, which is suited for integration into automated or in-line monitoring systems. The findings open up new possibilities in inkjet printing, e.g. real-time characterisation of ink viscosity and/or surface tension during jetting [42, 64], or on biomedical diagnostics with rapid small-volume property checks [65], of on other industrial processes with on-the-fly materials characterization [66].

By making our dataset (and code) openly available to the community, we expect that the database and models will be extended and potentially improved by including numerically obtained results and additional experiments under conditions not attainable in our facilities, thereby broadening validation and improving generalization.

DATA AVAILABILITY

The data and codes used in this study are openly available at: <https://github.com/CFTL-Illinois/Droplet-Properties-Prediction>.

ACKNOWLEDGMENTS

This work was supported by UCL’s Engineering and Physical Sciences Research Council (EPSRC) Impact Acceleration Account 2022-25. AAC-P acknowledges funding support from the UK Natural Environment Research Council (UKRI1271) and the UK Engineering and Physical Sciences Research Council (EP/W016036/1).

Appendix A: Convolutional Autoencoder Architecture

The droplet-breakup silhouettes used in this study contain fine-scale interface curvatures that must be encoded in a compact numerical representation. To achieve this, we trained a convolutional autoencoder that maps each padded grayscale droplet image of size 875×875 pixels into a 14-dimensional latent vector, which is later used

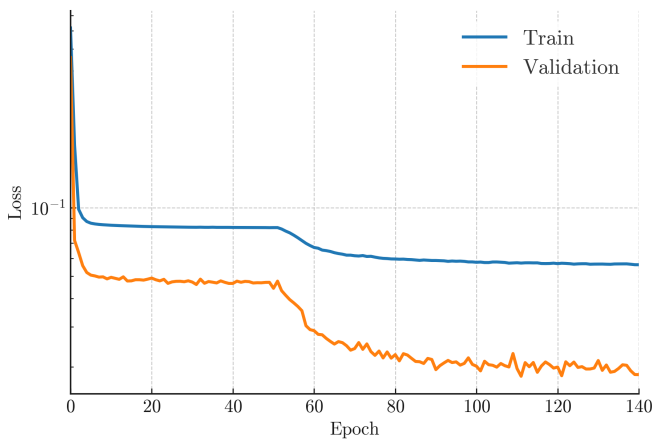


FIG. 11: Training and validation loss curves of the autoencoder. Early stopping is triggered at epoch 140.

as an input feature for the supervised and unsupervised learning models.

Table II lists the encoder–decoder parameters. The encoder progressively downsamples the image through six stride-2 convolutional layers, increasing the channel depth while reducing the spatial resolution. After flattening, a fully connected layer outputs a latent representation $z \in \mathbb{R}^{14}$. The decoder mirrors this structure: a fully connected expansion restores the spatial dimensions, followed by six transposed convolution layers that reconstruct the original 875×875 image.

The training and validation loss curves seen in Fig. 11 indicate a stable convergence. Early stopping is triggered at epoch 140 to obtain an accurate reconstruction without overfitting.

Appendix B: Supervised Learning Models

Four supervised models were trained to map droplet images and physical parameters to quantitative fluid properties. Models 1–3 predict viscosity and/or surface tension from measured physical variables and the 14-dimensional latent vectors produced by the convolutional autoencoder. In contrast, Model 4 performs the inverse task: it predicts the droplet’s latent geometric descriptor directly from five physical variables, enabling comparisons between experimental outcomes and shape embeddings. Fig. 12 shows a schematic multilayer perceptron (MLP) framework used for Models 1–4. Each model uses a fully connected architecture with seven hidden layers and ReLU activation functions, but differs in the dimensionality of its input and output spaces.

Appendix C: Clustering Algorithms

Here, we summarize the mathematical formulation of the clustering methods, i.e. the K -means and the Gaus-

sian mixture (GMM) algorithms. Both methods operate on the latent representations $z_i \in \mathbb{R}^{14}$ that were extracted from the convolutional autoencoder.

1. K -Means Clustering

The K -means algorithm partitions latent vectors $\{z_i\}_{i=1}^N$ into K clusters by minimizing the within-cluster sum of squared distances:

$$J(\{\mu_k\}, \{c_i\}) = \sum_{i=1}^N \|z_i - \mu_{c_i}\|^2, \quad (\text{C1})$$

where $c_i \in \{1, \dots, K\}$ is the assignment of sample i and $\mu_k \in \mathbb{R}^d$ is the centroid of cluster k .

a. Assignment step

Each data point is assigned to the nearest centroid:

$$c_i^{(t+1)} = \arg \min_k \|z_i - \mu_k^{(t)}\|^2. \quad (\text{C2})$$

b. Update step

Each centroid is updated as the mean of its assigned samples:

$$\mu_k^{(t+1)} = \frac{\sum_{i: c_i^{(t+1)}=k} z_i}{|\{i: c_i^{(t+1)}=k\}|}. \quad (\text{C3})$$

Iterations terminate when neither assignments nor centroids change appreciably.

2. Gaussian Mixture Models and the EM Algorithm

A Gaussian mixture model with K components represents the probability density of a latent vector $z \in \mathbb{R}^d$ as

$$p(z | \Theta) = \sum_{k=1}^K \pi_k \mathcal{N}(z | \mu_k, \Sigma_k), \quad (\text{C4})$$

where π_k are the mixture weights ($\pi_k \geq 0$, $\sum_k \pi_k = 1$), $\mu_k \in \mathbb{R}^d$ are the component means, and $\Sigma_k \in \mathbb{R}^{d \times d}$ are covariance matrices. The parameters $\Theta = \{\pi_k, \mu_k, \Sigma_k\}_{k=1}^K$ are estimated by maximizing the log-likelihood

$$\mathcal{L}(\Theta) = \sum_{i=1}^N \log p(z_i | \Theta). \quad (\text{C5})$$

Because the likelihood admits no closed-form maximizer, the EM algorithm is used to construct a sequence of estimates $\Theta^{(t)}$ that monotonically increases \mathcal{L} .

| Encoder | Operation |
|-------------------|--|
| Input | $875 \times 875 \times 1$ grayscale image (padded) |
| Conv Layer 1 | Conv2d(1, 32, kernel=5, stride=2, padding=2), ReLU |
| Conv Layer 2 | Conv2d(32, 64, kernel=5, stride=2, padding=2), ReLU |
| Conv Layer 3 | Conv2d(64, 128, kernel=5, stride=2, padding=2), ReLU |
| Conv Layer 4 | Conv2d(128, 256, kernel=5, stride=2, padding=2), ReLU |
| Conv Layer 5 | Conv2d(256, 256, kernel=5, stride=2, padding=2), ReLU |
| Conv Layer 6 | Conv2d(256, 256, kernel=5, stride=2, padding=2), ReLU |
| Flatten | Converts $256 \times 14 \times 14$ to vector |
| FC Layer | Linear($256 \cdot 14 \cdot 14 \rightarrow 14$) \Rightarrow latent vector z |
| Decoder | Operation |
| Input | Latent vector $z \in \mathbb{R}^{14}$ |
| FC Layer | Linear($14 \rightarrow 256 \cdot 14 \cdot 14$), ReLU |
| Reshape | $256 \times 14 \times 14$ |
| Transposed Conv 1 | ConvTranspose2d(256, 256, kernel=5, stride=2, padding=2, output_padding=1), ReLU |
| Transposed Conv 2 | ConvTranspose2d(256, 256, kernel=5, stride=2, padding=2, output_padding=1), ReLU |
| Transposed Conv 3 | ConvTranspose2d(256, 128, kernel=5, stride=2, padding=2, output_padding=1), ReLU |
| Transposed Conv 4 | ConvTranspose2d(128, 64, kernel=5, stride=2, padding=2, output_padding=1), ReLU |
| Transposed Conv 5 | ConvTranspose2d(64, 32, kernel=5, stride=2, padding=2, output_padding=1), ReLU |
| Transposed Conv 6 | ConvTranspose2d(32, 1, kernel=6, stride=2, padding=2, output_padding=1), Sigmoid |
| Output | Reconstructed image ($875 \times 875 \times 1$) |

TABLE II: Convolutional autoencoder architecture used for the droplet silhouette compression. The encoder reduces the input image to a 14-dimensional latent vector, and the decoder reconstructs the full-resolution image from the latent vector.

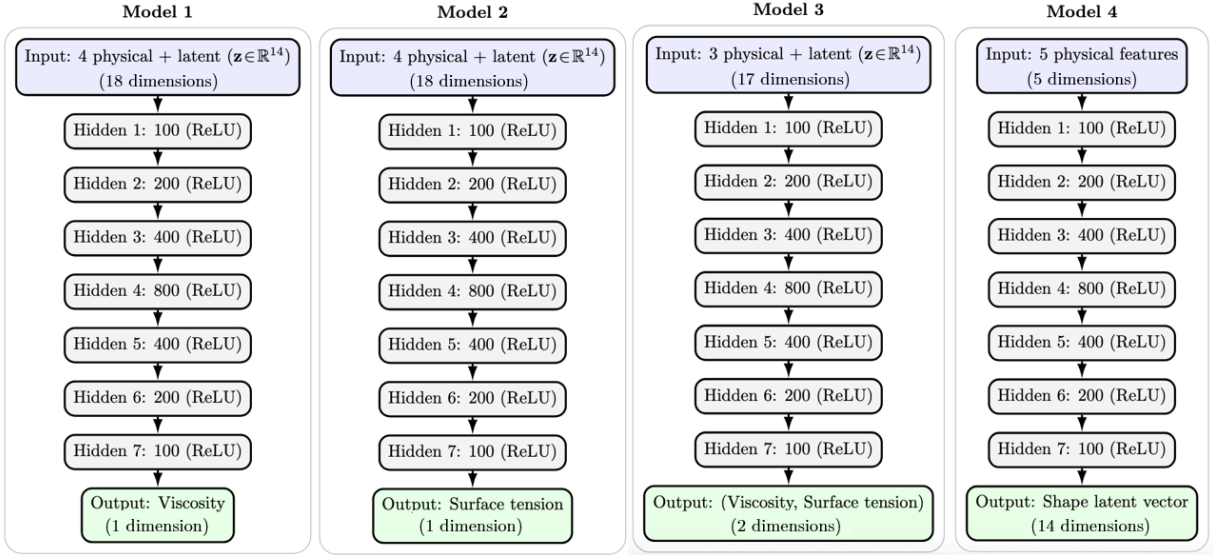


FIG. 12: Architecture summary of the supervised MLP models used in this work. Depending on the task, the inputs consist of physical parameters and, when required, the 14-dimensional latent droplet representation. The models predict viscosity (model 1), surface tension (model 2), viscosity and surface tension (model 3), or the 14-dimensional shape descriptor (model 4).

a. *E-step*

The posterior responsibility assigned to each mixture component k for a data point z_i is given by

$$\gamma_{ik}^{(t)} = \frac{\pi_k^{(t)} \mathcal{N}(z_i | \mu_k^{(t)}, \Sigma_k^{(t)})}{\sum_{j=1}^K \pi_j^{(t)} \mathcal{N}(z_i | \mu_j^{(t)}, \Sigma_j^{(t)})}, \quad (\text{C6})$$

with these values satisfying $0 \leq \gamma_{ik} \leq 1$ and $\sum_{k=1}^K \gamma_{ik} = 1$.

b. *M*-step

The effective membership of component k is

$$N_k^{(t+1)} = \sum_{i=1}^N \gamma_{ik}^{(t)}. \quad (\text{C7})$$

The updated mixture weights, means, and covariances are given by:

$$\pi_k^{(t+1)} = \frac{N_k^{(t+1)}}{N}, \quad (\text{C8})$$

$$\mu_k^{(t+1)} = \frac{\sum_{i=1}^N \gamma_{ik}^{(t)} z_i}{N_k^{(t+1)}}, \quad (\text{C9})$$

$$\Sigma_k^{(t+1)} = \frac{\sum_{i=1}^N \gamma_{ik}^{(t)} (z_i - \mu_k^{(t+1)})(z_i - \mu_k^{(t+1)})^T}{N_k^{(t+1)}}. \quad (\text{C10})$$

Iterations continue until the increase in log-likelihood drops below a specified threshold.

Appendix D: Cluster Evaluation Results

We evaluated two standard metrics for both the K-Means and the Gaussian mixture models, i.e., the Silhouette Score and the Davies–Bouldin Index. These metrics provide complementary assessments of how well the data partition into distinct clusters for a given choice of K .

Figure 13a shows the Silhouette Score as a function of the cluster number K . The score measures the relative separation between clusters: values closer to 1 indicate samples that are well matched to their own cluster and poorly matched to neighboring clusters. Both K-Means and GMM exhibit nearly identical trends, with the score increasing from $K = 2$ to 5 and reaching a broad maximum in this range. This behavior suggests that the learned latent manifold naturally organizes the droplet silhouettes into a moderate number of distinct morphological families. Increasing K beyond this range yields only marginal improvement, indicating that additional splitting does not reveal further meaningful structure.

Figure 13b presents the DBI, which quantifies the average similarity between each cluster and its most similar neighbor. Lower DBI values correspond to better-defined, more separated clusters. Consistent with the Silhouette analysis, the DBI decreases sharply from $K = 2$ to $K = 5$ –6 for both algorithms, after which improvements saturate. The close agreement between K-Means and GMM across both metrics reinforces the stability of the cluster structure and indicates that the latent space provides a robust embedding in which fluid composition and interfacial behavior are reflected as geometric regularities.

These two metrics show that $K \approx 5$ provides an optimal balance between cluster compactness and separation, matching the visual grouping observed in the latent-space

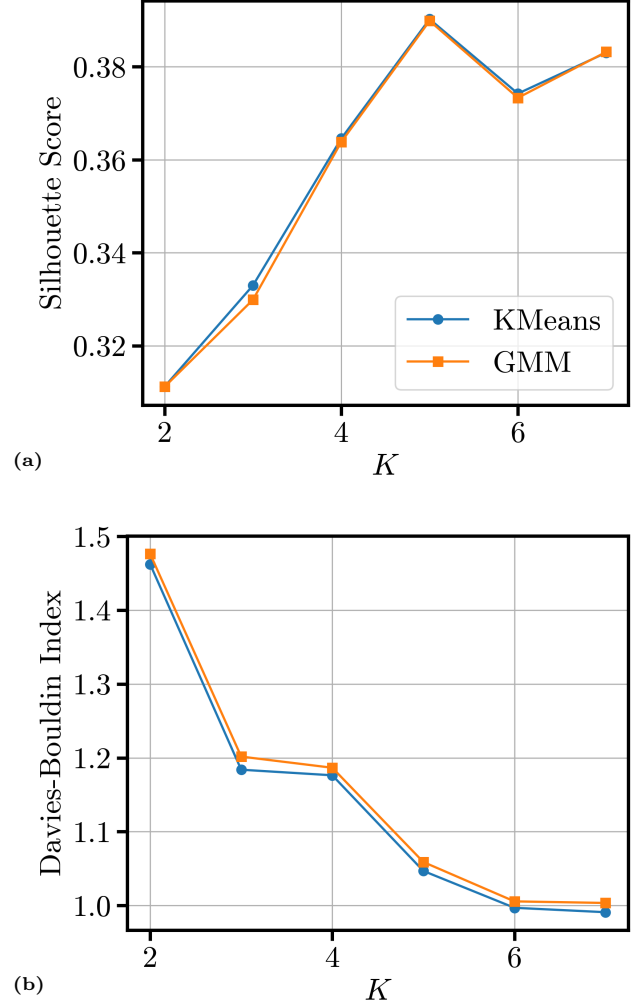


FIG. 13: Cluster evaluation results. (a) Silhouette Scores for K-Means and GMM across cluster sizes K . (b) Davies–Bouldin Index (DBI) for K-Means and GMM across K .

projections and supporting the use of five-cluster partitioning in the analysis of droplet breakup regimes.

Appendix E: K-means and GMM Cluster Assignments

This section reports the full cluster assignment counts for the liquids tested in the dataset. Tables III and IV provide a fine-grained view of liquid formulation distributions across the five clusters obtained from the K-means and Gaussian mixture models. As observed, highly viscous liquids—including pure glycerin and silicone oils of 350 cSt and 1000 cSt—largely occupy cluster 4, reflecting their well-separated breakup behavior in the latent and physical parameter spaces. Conversely, low-viscosity

| Liquid type | cluster | | | | |
|--------------------------|---------|----|----|----|----|
| | 0 | 1 | 2 | 3 | 4 |
| 10% water + 90% ethanol | 10 | 5 | 5 | 10 | 0 |
| 10% water + 90% glycerin | 1 | 5 | 0 | 5 | 14 |
| 20% water + 80% glycerin | 18 | 8 | 18 | 10 | 0 |
| 30% water + 70% ethanol | 10 | 5 | 5 | 10 | 0 |
| 30% water + 70% glycerin | 5 | 5 | 10 | 10 | 0 |
| 40% water + 60% glycerin | 8 | 9 | 18 | 19 | 0 |
| 5% water + 95% ethanol | 10 | 5 | 5 | 10 | 0 |
| 5% water + 95% glycerin | 4 | 5 | 0 | 1 | 15 |
| 50% water + 50% ethanol | 10 | 5 | 5 | 10 | 0 |
| 50% water + 50% glycerin | 0 | 10 | 13 | 18 | 0 |
| 70% water + 30% ethanol | 10 | 5 | 9 | 6 | 0 |
| 70% water + 30% glycerin | 0 | 10 | 12 | 10 | 0 |
| 80% water + 20% ethanol | 14 | 9 | 18 | 18 | 0 |
| 90% water + 10% ethanol | 4 | 5 | 10 | 11 | 0 |
| 90% water + 10% glycerin | 0 | 10 | 11 | 10 | 0 |
| Pure glycerin | 0 | 0 | 0 | 2 | 28 |
| Methanol | 19 | 9 | 9 | 17 | 0 |
| Pure ethanol | 20 | 9 | 9 | 16 | 0 |
| Pure water | 0 | 16 | 10 | 10 | 0 |
| Silicone oil 1000 cSt | 0 | 0 | 0 | 0 | 8 |
| Silicone oil 2 cSt | 15 | 5 | 5 | 5 | 0 |
| Silicone oil 350 cSt | 0 | 0 | 0 | 0 | 18 |
| Silicone oil 50 cSt | 0 | 9 | 9 | 0 | 36 |
| Silicone oil 5 cSt | 17 | 5 | 5 | 3 | 0 |

TABLE III: K-means cluster assignment counts for all liquid types.

| Liquid type | cluster | | | | |
|--------------------------|---------|----|----|----|----|
| | 0 | 1 | 2 | 3 | 4 |
| 10% water + 90% ethanol | 10 | 5 | 5 | 10 | 0 |
| 10% water + 90% glycerin | 1 | 5 | 0 | 5 | 14 |
| 20% water + 80% glycerin | 18 | 9 | 18 | 9 | 0 |
| 30% water + 70% ethanol | 10 | 5 | 5 | 10 | 0 |
| 30% water + 70% glycerin | 5 | 5 | 10 | 10 | 0 |
| 40% water + 60% glycerin | 8 | 9 | 18 | 19 | 0 |
| 5% water + 95% ethanol | 10 | 5 | 5 | 10 | 0 |
| 5% water + 95% glycerin | 4 | 5 | 0 | 1 | 15 |
| 50% water + 50% ethanol | 10 | 5 | 5 | 10 | 0 |
| 50% water + 50% glycerin | 0 | 10 | 13 | 18 | 0 |
| 70% water + 30% ethanol | 10 | 5 | 9 | 6 | 0 |
| 70% water + 30% glycerin | 0 | 10 | 12 | 10 | 0 |
| 80% water + 20% ethanol | 14 | 9 | 18 | 18 | 0 |
| 90% water + 10% ethanol | 4 | 5 | 10 | 11 | 0 |
| 90% water + 10% glycerin | 0 | 10 | 11 | 10 | 0 |
| Pure glycerin | 0 | 0 | 0 | 2 | 28 |
| Methanol | 18 | 9 | 9 | 18 | 0 |
| Pure ethanol | 18 | 9 | 9 | 18 | 0 |
| Pure water | 0 | 16 | 10 | 10 | 0 |
| Silicone oil 1000 cSt | 0 | 0 | 0 | 0 | 8 |
| Silicone oil 2 cSt | 15 | 5 | 5 | 5 | 0 |
| Silicone oil 350 cSt | 0 | 0 | 0 | 0 | 18 |
| Silicone oil 50 cSt | 0 | 9 | 9 | 0 | 36 |
| Silicone oil 5 cSt | 17 | 5 | 5 | 3 | 0 |

TABLE IV: GMM cluster assignment counts for all liquid types.

mixtures largely populate cluster 0, consistent with their overlapping regimes in the $Bo-Oh$ and $Re-Oh$ diagrams.

-
- [1] A. L. Dearden, P. J. Smith, D.-Y. Shin, N. Reis, B. Derby, and P. O'Brien, A low curing temperature silver ink for use in ink-jet printing and subsequent production of conductive tracks, *Macromolecular Rapid Communications* **26**, 315 (2005).
- [2] J. Stringer and B. Derby, Limits to feature size and resolution in ink jet printing, *Journal of the European Ceramic Society* **29**, 913 (2009).
- [3] S. Pan, R. Guo, M. Björnalm, J. J. Richardson, L. Li, C. Peng, N. Bertleff-Zieschang, W. Xu, J. Jiang, and F. Caruso, Coatings super-repellent to ultralow surface tension liquids, *Nature materials* **17**, 1040 (2018).
- [4] T. Carey, C. Jones, F. Le Moal, D. Deganello, and F. Torrisi, Spray-coating thin films on three-dimensional surfaces for a semitransparent capacitive-touch device, *ACS applied materials & interfaces* **10**, 19948 (2018).
- [5] C. E. Stauffer, The measurement of surface tension by the pendant drop technique, *The journal of physical chemistry* **69**, 1933 (1965).
- [6] S. M. Saad, Z. Policova, and A. W. Neumann, Design and accuracy of pendant drop methods for surface tension measurement, *Colloids and Surfaces A: Physicochemical and Engineering Aspects* **384**, 442 (2011).
- [7] F. Bashforth and J. C. Adams, *An attempt to test the theories of capillary action: by comparing the theoretical and measured forms of drops of fluid* (University Press, 1883).
- [8] F. Hansen and G. Rødstrud, Surface tension by pendant drop: I. a fast standard instrument using computer image analysis, *Journal of colloid and interface science* **141**, 1 (1991).
- [9] J. D. Berry, M. J. Neeson, R. R. Dagastine, D. Y. Chan, and R. F. Tabor, Measurement of surface and interfacial tension using pendant drop tensiometry, *Journal of colloid and interface science* **454**, 226 (2015).
- [10] S.-Y. Lin, L.-J. Chen, J.-W. Xyu, and W.-J. Wang, An examination on the accuracy of interfacial tension measurement from pendant drop profiles, *Langmuir* **11**, 4159 (1995).
- [11] S.-Y. Lin, W.-J. Wang, L.-W. Lin, and L.-J. Chen, Systematic effects of bubble volume on the surface tension measured by pendant bubble profiles, *Colloids and Surfaces A: Physicochemical and Engineering Aspects* **114**, 31 (1996).
- [12] A. Morita, D. Carastan, and N. Demarquette, Influence of drop volume on surface tension evaluated using the pendant drop method, *Colloid and Polymer Science* **280**, 857 (2002).
- [13] W. D. Harkins and H. F. Jordan, A method for the determination of surface and interfacial tension from the maximum pull on a ring, *Journal of the American Chemical Society* **52**, 1751 (1930).
- [14] M. Simon, Recherches sur la capillarité, in *Annales de Chimie et de Physique*, Vol. 32 (1851) p. 5.
- [15] N. Dixit, D. L. Zeng, and D. S. Kalonia, Application of maximum bubble pressure surface tensiometer to study protein-surfactant interactions, *International journal of pharmaceutics* **439**, 317 (2012).
- [16] V. Fainerman and R. Miller, Maximum bubble pressure tensiometry—an analysis of experimental constraints, *Advances in colloid and interface science* **108**, 287 (2004).
- [17] C. Weber, Zum zerfall eines flüssigkeitsstrahles, *ZAMM-Journal of Applied Mathematics and Mechanics/Zeitschrift für Angewandte Mathematik und Mechanik* **11**, 136 (1931).
- [18] A. Gaillard, R. Sijs, and D. Bonn, What determines the drop size in sprays of polymer solutions?, *Journal of non-Newtonian fluid mechanics* **305**, 104813 (2022).
- [19] J. R. Castrejón-Pita, A. A. Castrejón-Pita, S. S. Thete, K. Sambath, I. M. Hutchings, J. Hinch, J. R. Lister, and O. A. Basaran, Plethora of transitions during breakup of liquid filaments, *Proceedings of the National Academy of Sciences* **112**, 4582 (2015).
- [20] G. Schramm *et al.*, A practical approach to rheology and rheometry, . (1994).
- [21] E. P. Koehler, D. W. Fowler, C. F. Ferraris, and S. Amziane, A new, portable rheometer for fresh self-consolidating concrete, *ACI SPECIAL PUBLICATIONS* **233**, 97 (2005).
- [22] A. Castrejón-Pita, E. Betton, N. Campbell, N. Jackson, J. Morgan, T. Tuladhar, D. Vadillo, and J. R. Castrejón-Pita, Formulation, quality, cleaning, and other advances in inkjet printing, *Atomization and Sprays* **31** (2021).
- [23] A. A. Castrejón-Pita, J. Castrejón-Pita, and I. Hutchings, Breakup of liquid filaments, *Physical review letters* **108**, 074506 (2012).
- [24] O. A. Basaran, H. Gao, and P. P. Bhat, Nonstandard inkjets, *Annual Review of Fluid Mechanics* **45**, 85 (2013).
- [25] O. A. Basaran, Small-scale free surface flows with breakup: Drop formation and emerging applications, *American Institute of Chemical Engineers. AIChE Journal* **48**, 1842 (2002).
- [26] R. F. Day, E. J. Hinch, and J. R. Lister, Self-similar capillary pinch-off of an inviscid fluid, *Physical review letters* **80**, 704 (1998).
- [27] J. Castrejón-Pita, A. A. Castrejón-Pita, E. Hinch, J. R. Lister, and I. M. Hutchings, Self-similar breakup of near-inviscid liquids, *Phys. Rev. E* **86**, 015301 (2012).
- [28] J. B. Keller and M. J. Miksis, Surface tension driven flows, *SIAM Journal on Applied Mathematics* **43**, 268 (1983).
- [29] A. U. Chen, P. K. Notz, and O. A. Basaran, Computational and experimental analysis of pinch-off and scaling, *Physical review letters* **88**, 174501 (2002).
- [30] D. T. Papageorgiou, On the breakup of viscous liquid threads, *Physics of fluids* **7**, 1529 (1995).
- [31] J. Eggers, Universal pinching of 3d axisymmetric free-surface flow, *Physical review letters* **71**, 3458 (1993).
- [32] Y. Li and J. E. Sprittles, Capillary breakup of a liquid bridge: identifying regimes and transitions, *Journal of Fluid Mechanics* **797**, 29 (2016).
- [33] B. Ambravaneswaran, H. J. Subramani, S. D. Phillips, and O. A. Basaran, Dripping-jetting transitions in a dripping faucet, *Physical review letters* **93**, 034501 (2004).
- [34] P. K. Notz and O. A. Basaran, Dynamics and breakup of a contracting liquid filament, *Journal of Fluid Mechanics* **512**, 223 (2004).
- [35] D. Alveringh, D. Le, J. Groenesteijn, J. Schmitz, and J. Lötters, Fluid classification with integrated flow and pressure sensors using machine learning, *Sensors and Actuators A: Physical* **363**, 114762 (2023).

- [36] Q. Chen, A. Castillo-Castellanos, and C. R. Constante-Amores, Dynamics of a data-driven low-dimensional model of rayleigh–bénard convection, arXiv preprint (2025), arXiv:2507.11858 [physics.flu-dyn].
- [37] C. R. Constante-Amores, A. J. Linot, and M. D. Graham, Dynamics of a data-driven low-dimensional model of turbulent minimal pipe flow (2025), arXiv:2408.03135 [physics.flu-dyn].
- [38] A. Gaikwad, T. Chang, B. Giera, N. Watkins, S. Mukherjee, A. Pascall, D. Stobbe, and P. Rao, In-process monitoring and prediction of droplet quality in droplet-on-demand liquid metal jetting additive manufacturing using machine learning, *Journal of Intelligent Manufacturing* **33**, 2093 (2022).
- [39] H. Chen, Y. Liu, S. Balabani, R. Hirayama, and J. Huang, Machine learning in predicting printable bio-material formulations for direct ink writing, *Research* **6**, 0197 (2023).
- [40] F. S. Kratz and J. Kierfeld, Pendant drop tensiometry: A machine learning approach, *The Journal of Chemical Physics* **153**, 094701 (2020).
- [41] T. Li, L. Lu, Q. Zeng, and K. Liao, Machine learning based multi-parameter droplet optimisation model study, *Scientific Reports* **15**, 25966 (2025).
- [42] S. Kim, M. Cho, and S. Jung, The design of an inkjet drive waveform using machine learning, *Scientific Reports* **12**, 4841 (2022).
- [43] P. S. Clegg, Characterising soft matter using machine learning, *Soft Matter* **17**, 3991 (2021).
- [44] T. Orlova, A. Piven, D. Darmoroz, T. Aliev, T. M. T. A. Razik, A. Boitsev, N. Grafeeva, and E. Skorb, Machine learning for soft and liquid molecular materials, *Digital Discovery* **2**, 298 (2023).
- [45] M. H. Mobarak, M. A. Mimona, M. A. Islam, N. Hossain, F. T. Zohura, I. Imtiaz, and M. I. H. Rimon, Scope of machine learning in materials research—a review, *Applied Surface Science Advances* **18**, 100523 (2023).
- [46] J. Masci, U. Meier, D. Cireşan, and J. Schmidhuber, Stacked convolutional auto-encoders for hierarchical feature extraction, in *International conference on artificial neural networks* (Springer, 2011) pp. 52–59.
- [47] J. W. Khor, N. Jean, E. S. Luxenberg, S. Ermon, and S. K. Tang, Using machine learning to discover shape descriptors for predicting emulsion stability in a microfluidic channel, *Soft matter* **15**, 1361 (2019).
- [48] H. Zhang and S. K. Moon, Reviews on machine learning approaches for process optimization in noncontact direct ink writing, *ACS Applied Materials & Interfaces* **13**, 53323 (2021).
- [49] L. Au-Yeung and P. A. Tsai, Predicting impact outcomes and maximum spreading of drop impact on heated nanostructures using machine learning, *Langmuir* **39**, 18327 (2023).
- [50] M. Tembely, D. C. Vadillo, A. Dolatabadi, and A. Soucemarianadin, A machine learning approach for predicting the maximum spreading factor of droplets upon impact on surfaces with various wettabilities, *Processes* **10**, 1141 (2022).
- [51] M. Pierzyna, D. A. Burzynski, S. E. Bansmer, and R. Semaan, Data-driven splashing threshold model for drop impact on dry smooth surfaces, *Physics of Fluids* **33** (2021).
- [52] S. Kim, R. Wenger, O. Bürgy, G. Balestra, U. Jeong, and S. Jung, Predicting inkjet jetting behavior for viscoelastic inks using machine learning, *Flexible and Printed Electronics* **8**, 035007 (2023).
- [53] S. Kim, M. Cho, and S. Jung, Reinforcement learning-based dynamic optimization of driving waveforms for inkjet printing of viscoelastic fluids, *Langmuir* **41**, 10831 (2025).
- [54] K. J. Mysels, Some limitations in the interpretation of the time dependence of surface tension measured by the maximum bubble pressure method, *Langmuir* **5**, 442 (1989).
- [55] N. Otsu *et al.*, A threshold selection method from gray-level histograms, *Automatica* **11**, 23 (1975).
- [56] D. P. Kingma, Adam: A method for stochastic optimization, arXiv preprint arXiv:1412.6980 (2014).
- [57] A. Creswell, K. Arulkumaran, and A. A. Bharath, On denoising autoencoders trained to minimise binary cross-entropy (2017), arXiv:1708.08487 [cs.CV].
- [58] T. Chen and C. Guestrin, Xgboost: A scalable tree boosting system, in *Proceedings of the 22nd ACM SIGKDD International Conference on Knowledge Discovery and Data Mining*, KDD '16 (ACM, 2016) p. 785–794.
- [59] P. J. Rousseeuw, Silhouettes: a graphical aid to the interpretation and validation of cluster analysis, *Journal of computational and applied mathematics* **20**, 53 (1987).
- [60] D. L. Davies and D. W. Bouldin, A cluster separation measure, *IEEE transactions on pattern analysis and machine intelligence* , 224 (2009).
- [61] D. Lohse, Fundamental fluid dynamics challenges in inkjet printing, *Annual review of fluid mechanics* **54**, 349 (2022).
- [62] L. Bautista, D. C. Vargas, X. Luo, *et al.*, A simple capillary viscometer based on the ideal gas law, *RSC advances* **8**, 30441 (2018).
- [63] N. Seimiya and K. Takei, Simultaneous measurement of surface tension and viscosity using a liquid dynamics sensor, *Small Methods* , 2401983 (2025).
- [64] T. H. Phung, S. H. Park, I. Kim, T.-M. Lee, and K.-S. Kwon, Machine learning approach to monitor inkjet jetting status based on the piezo self-sensing, *Scientific Reports* **13**, 18089 (2023).
- [65] P. S. Lenzen, F. Dingfelder, M. Muller, and P. Arosio, Portable microfluidic viscometer for formulation development and in situ quality control of protein and antibody solutions, *Analytical Chemistry* **96**, 13185 (2024).
- [66] S. Tronci, P. Van Neer, E. Giling, U. Stelwagen, D. Piras, R. Mei, F. Corominas, and M. Grosso, In-line monitoring and control of rheological properties through data-driven ultrasound soft-sensors, *Sensors* **19**, 5009 (2019).